

A study of differentiation errors in large-eddy simulations based on the EDQNM theory

J. Berland^{a,*}, C. Bogey^b, C. Bailly^b

^a SINUMEF, Arts et Métier ParisTech, 151 Boulevard de l'Hôpital, 75013 Paris, France

^b LMFA, UMR CNRS 5509, École Centrale de Lyon, 36 Avenue Guy de Collongue, 69134 Ecully, France

ARTICLE INFO

Article history:

Received 10 December 2007

Received in revised form 13 May 2008

Accepted 24 May 2008

Available online 11 June 2008

Keywords:

Large-eddy simulation

Numerical error

EDQNM theory

Approximate differentiation

ABSTRACT

This paper is concerned with the investigation of numerical errors in large-eddy simulations by means of two-point turbulence modeling. Based on the eddy-damped quasi-normal Markovian (EDQNM) theory, a stochastic model is developed in order to predict the time evolution of the kinetic energy spectrum obtained by a large-eddy simulation (LES), including the effects of the numerics. Using this framework, the influence of the accuracy of the approximate space differencing schemes on LES quality is studied, for decaying homogeneous isotropic incompressible turbulence, with Reynolds numbers Re_τ based on the transverse Taylor scale equal to 780, 2500 and 8000. The results show that the discretization of the filtered Navier–Stokes equations leads to differentiation and aliasing errors. Error spectra are also presented, and indicate that the numerical errors are mainly originating from the approximate differentiation. In addition, increasing the order of accuracy of the differencing schemes or using algorithms optimized in the Fourier space is found to widen the range of well-resolved scales. Unfortunately, for all the schemes, the smaller scales with wavenumbers close to the grid cut-off wavenumber, are badly calculated and generate differentiation errors over the whole energy spectrum. The eventual use of explicit filtering to remove spurious motions with short wavelength is finally shown to significantly improve LES accuracy.

© 2008 Elsevier Inc. All rights reserved.

1. Introduction

Numerical solutions of turbulent flow problems can be accomplished using various levels of approximation. For direct numerical simulations (DNS), the full Navier–Stokes equations are solved and, assuming that the time step and the mesh size are small enough, the whole range of turbulence scales are computed. The method is particularly reliable since it does not require physical modeling, but on the other hand resolving all the turbulent scales is highly demanding in term of computational cost. An alternative approach needing less computational efforts is large-eddy simulation (LES). In LES, only the larger scales are solved while the effects of the scales smaller than the mesh size are taken into account through a subgrid scale (SGS) model [1]. Since the early works of Smagorinsky [2], numerous SGS models have been proposed with the aim of describing the behaviour of unresolved scales based on the knowledge of the resolved velocity field. The reader may refer to the review of Lesieur and Métais [3] for an overview of LES techniques for incompressible flows.

A large variety of SGS modeling procedures have been derived by applying physical assumptions to the filtered Navier–Stokes equations, without mentioning the discretization methods. LES performed using explicit models for the subgrid motions, and where negligible numerical errors is assumed, are referred to as *pure physical LES* by Pope [4]. The numerical accu-

* Corresponding author. Fax: +33 1 44 24 62 75.

E-mail address: julien.berland@paris.ensam.fr (J. Berland).

racy in the framework of LES is however a delicate issue. The investigation of discretization errors indeed commonly depends on the intrinsic properties of the discretization schemes. The formal order of accuracy of a differencing scheme yields the difference between the exact and the approximate derivatives as the mesh size tends to zero. In a similar manner, the effective wavenumber provides the errors in the Fourier space introduced for a simple derivative [5]. Considering this, there is unfortunately no straightforward link between the quality of a LES calculation and the resolution ability of the discretization tools in simple canonical problems. Grid convergence is for example not ensured. Using a smaller grid size indeed shifts the cut-off wavenumber to smaller scales which can still carry a significant amount of energy.

The investigation of numerical errors in LES requires the design of accuracy estimators combining the numerical procedures and the physical model based on the filtered Navier–Stokes equations. A first extensive theoretical framework allowing quantitative evaluation of numerical errors in LES has been proposed by Ghosal [6] and has been referred to as *static error analysis* later on by Park and Mahesh [7]. The static error analysis provides a formal model in the spectral space of the numerical implementation of a LES. The errors are then given by the deviation of the numerical system from the exact model, and the error spectra are computed assuming a Gaussian state for the velocity field. Two major sources of errors, namely approximate differentiation and aliasing, have been identified by Ghosal [6], who also found that 2nd-order discretization schemes introduce errors larger than the SGS terms. A filter with a filter-size-to-grid-width ratio of 8 then needs to be implemented to remove poorly resolved scales. Ghosal [6] showed in addition that for eight-order schemes a filter width twice as large as the grid size is enough to ensure numerical accuracy. High-order algorithms hence turn out to be more appropriate. This trend has been further supported by the *a priori* analysis of DNS data achieved by Chow and Moin [8] for stably stratified homogeneous flows, which concluded that high-order numerical methods allow a wider range of accuracy in terms of length scales supported by the grid. Similarly, the LES of turbulent channel flows performed by Krachvenko and Moin [9] indicated that the performance of subgrid scale models can be improved by increasing the order of the finite-difference schemes.

Even if the static error analysis provides insightful details on numerical errors in LES, the method does not fully reproduce the variety of phenomena involved in simulations. In particular, as pointed out by Park and Mahesh [7], dynamical interactions cannot be taken into account with a static approach. A *dynamic error analysis* can nevertheless be performed by applying the eddy-damped quasi-normal Markovian (EDQNM) set of hypothesis to the LES approach in order to design a so-called “EDQNM-LES” model [7]. This theoretical framework enables to compute the time evolution of the kinetic energy spectrum obtained by a LES, including the effects of the numerical methods, for incompressible homogeneous isotropic turbulence. The EDQNM-LES approach has been used to study numerical errors by Park and Mahesh [7]. Their works are however mainly based on the Comte-Bellot and Corrsin [10] experiment which is a low Reynolds number flow configuration ($Re_\lambda = 70$), and briefly deal with LES at high Reynolds number.

The present study is an attempt to provide a parametric study of the influence of the accuracy of the discretization algorithms on numerical errors in LES. Following developments similar to those proposed by Park and Mahesh [7], an EDQNM-LES model is derived to evaluate the time evolution of kinetic energy spectra obtained from LES performed with numerical differentiation methods of orders of accuracy from 2 to 14, and with optimized finite-difference schemes [11].

The numerical errors in LES are considered for the three cases with Reynolds number Re_λ based on the transverse Taylor scale equal to 780, 2500 and 8000. The classical EDQNM theory, referred to as “EDQNM-DNS”, is applied to determine reference kinetic energy spectra. Both static and dynamic analysis are then carried out. Following Ghosal’s works [6], the numerical errors are first defined and computed by comparing the EDQNM-LES spectra to the EDQNM-DNS spectra (static error analysis). The results are recast in terms of accuracy limits using the SGS contribution as an acceptable upper bound for the numerical errors. To take into account the computational cost required by the discretization tools to reach a given accuracy, efficiency rates are also introduced to yield unbiased estimations of the scheme performance. Based on the study of Park and Mahesh [7], contributions from the SGS model, the approximate differentiation and aliasing are also introduced (dynamic error analysis). Their time evolutions are considered to evaluate whether numerical errors have a major impact on the solution quality. Accuracy improvement using explicit filtering is eventually discussed.

The LES is first considered in the physical space in Section 2 in order to introduce the numerical errors in a more intuitive manner than in the spectral space. In-depth developments of the numerical errors are carried out in Section 3 using the EDQNM-DNS and EDQNM-LES models. The reference solutions and the results of the EDQNM-LES calculations are shown in Section 4. Concluding remarks are finally drawn in Section 5.

2. Differentiation and aliasing errors in physical space

In LES, scale separation is performed so that only the non-universal large turbulent scales are computed. The definition of these large scales may vary from one model to another depending on how the scale separation is carried out. It can be explicit or implicit, and can rely on more or less sharp filters.

2.1. Implicit grid filtering

We first focus on LES with scale separation implicitly achieved by the projection of the velocity field on the mesh. The projection of a flow solution on a grid indeed introduces a spectral filtering of the flow variables at the cut-off wavenum-

ber $k_c = \pi/\Delta$ where Δ is the mesh size. Following Domaradzki and Adams [12] a notation explicitly involving this spectral truncation is proposed. It is denoted by the upper-script \mathcal{L} and its complement by \mathcal{S} . Flow variables are then decomposed as

$$f = f^{\mathcal{L}} + f^{\mathcal{S}}. \quad (1)$$

A generic one-dimensional transport equation is now considered

$$\frac{\partial u}{\partial t} + \frac{\partial}{\partial x} F(u) = 0, \quad (2)$$

where u corresponds to the velocity field and F is a nonlinear operator. The full incompressible Navier–Stokes equations are not used here for notational simplicity but the reasoning given in what follows for Eq. (2) is valid for them. Note nonetheless that the treatment of the pressure term can give rise to specific numerical errors [13].

The derivation of the formal model underlying the LES of system (2) is performed by applying a filtering operator (\mathcal{L} in the present framework). Assuming that filtering and differentiation commute, the governing equation for the filtered field reads

$$\frac{\partial u^{\mathcal{L}}}{\partial t} + \frac{\partial}{\partial x} F(u^{\mathcal{L}}) = \frac{\partial}{\partial x} [F(u^{\mathcal{L}}) - F(u)^{\mathcal{L}}], \quad (3)$$

where the right-hand side takes into account the effects of the unresolved scales on the resolved ones.

The practical implementation of a LES is nevertheless based on grid functions defined only at some grid points. The discretization is assumed to be carried out by an operator $[\cdot]_N$ which maps a continuous function into a set of discrete values at the grid nodes. It should be noted that the discretization operator $[\cdot]_N$ may generate aliasing errors when it is directly applied to quantities with a spectral content lying outside the wavenumber range supported by the mesh. The discretization of a quantity f indeed reads

$$[f]_N = [f^{\mathcal{L}}]_N + [f^{\mathcal{S}}]_N. \quad (4)$$

According to the definition of the projector \mathcal{L} , the first term on the right-hand side corresponds to the scales which can be correctly discretized on the mesh. However, the second term $[f^{\mathcal{S}}]_N$ contains only scales with wavenumbers higher than those supported by the mesh. The discretization of these components will produce aliasing, which will contaminate the resolved discretized variable $[f^{\mathcal{L}}]_N$ by spurious motions. Remark that LES only aim at calculating the resolved discretized field $[f^{\mathcal{L}}]_N$, also denoted in what follows by f_N .

The grid projection \mathcal{L} and the discretization operator $[\cdot]_N$ are now applied to the system (2) under consideration. Assuming that time integration is ideal enables to write the governing equation for the resolved discretized velocity field $[u^{\mathcal{L}}]_N = u_N$ as

$$\frac{\partial u_N}{\partial t} + \left[\frac{\partial}{\partial x} F(u)^{\mathcal{L}} \right]_N = 0. \quad (5)$$

Similarly to the formal model (3), further modeling is required for the nonlinear terms in (5). The commutation of the operators in the series $[\cdot]_N$, ∂_x , \mathcal{L} and F will allow us to express the quadratic interactions in term of u_N , but it will also generate commutation error terms resulting from discretization and modeling biases.

The commutation between the discretization $[\cdot]_N$ and the exact differentiation ∂_x requires to introduce an approximate derivative operator $\delta/\delta x$ such as

$$\left[\frac{\partial}{\partial x} F(u)^{\mathcal{L}} \right]_N = \frac{\delta}{\delta x} [F(u)^{\mathcal{L}}]_N - \underbrace{\left\{ \frac{\delta}{\delta x} [F(u)^{\mathcal{L}}]_N - \left[\frac{\partial}{\partial x} F(u)^{\mathcal{L}} \right]_N \right\}}_{R_{\text{rd}}(u)}, \quad (6)$$

where $R_{\text{rd}}(u)$ is the local truncation error.

The grid projection \mathcal{L} must then be introduced into the nonlinear terms of Eq. (6), i.e. the substitution of $F(u)^{\mathcal{L}}$ by $F(u^{\mathcal{L}})$ is performed using the relationship

$$[F(u)^{\mathcal{L}}]_N = [F(u^{\mathcal{L}})]_N + [F(u)^{\mathcal{L}} - F(u^{\mathcal{L}})]_N. \quad (7)$$

The spectral content of the quantity $F(u^{\mathcal{L}})$ is however not limited to the grid resolution. The aliasing errors and the SGS tensor are then both contained in the residual term $[F(u)^{\mathcal{L}} - F(u^{\mathcal{L}})]_N$. It is thus convenient to decompose $F(u^{\mathcal{L}})$ into its resolved and non-resolved parts, $F(u^{\mathcal{L}})^{\mathcal{L}}$ and $F(u^{\mathcal{L}})^{\mathcal{S}}$, so that the aliasing and the modeling issues can be separated:

$$[F(u)^{\mathcal{L}}]_N = [F(u^{\mathcal{L}})]_N + \underbrace{[F(u)^{\mathcal{L}} - F(u^{\mathcal{L}})]_N}_{\text{sgs}} + \underbrace{[-F(u^{\mathcal{L}})^{\mathcal{S}}]_N}_{\text{aliasing}}. \quad (8)$$

In this expression the term $[-F(u^{\mathcal{L}})^{\mathcal{S}}]_N$ indeed takes into account the unresolved part of the nonlinear terms introduced by $[F(u^{\mathcal{L}})]_N = [F(u^{\mathcal{L}})^{\mathcal{L}}]_N + [F(u^{\mathcal{L}})^{\mathcal{S}}]_N$. In addition, the SGS term compares the resolved fluxes computed with the full velocity field $F(u)^{\mathcal{L}}$, with the resolved fluxes obtained with the resolved velocity field $F(u^{\mathcal{L}})^{\mathcal{L}}$.

The last step consists in commuting the nonlinear operator F and the discretization $[\cdot]_N$. If the grid is assumed to be collocated and if finite-difference methods are implemented there is no issue of flux reconstruction and one can write that

$$[F(u^\mathcal{L})]_N = F_N([u^\mathcal{L}]_N) = F_N(u_N), \tag{9}$$

where F_N is the flux function acting on grid functions. Finally, the time evolution of the resolved discretized velocity field is given by

$$\frac{\partial u_N}{\partial t} + \frac{\delta}{\delta X} F_N(u_N) = R_{\text{sgs}}(u) + R_{\text{fd}}(u) + R_{\text{al}}(u) \tag{10}$$

with the residual terms:

$$R_{\text{sgs}}(u) = \frac{\delta}{\delta X} [F(u^\mathcal{L})^\mathcal{L} - F(u)^\mathcal{L}]_N, \tag{11}$$

$$R_{\text{fd}}(u) = \frac{\delta}{\delta X} [F(u)^\mathcal{L}]_N - \left[\frac{\partial}{\partial X} F(u)^\mathcal{L} \right]_N, \tag{12}$$

$$R_{\text{al}}(u) = \frac{\delta}{\delta X} [F(u^\mathcal{L})^\mathcal{L}]_N \tag{13}$$

corresponding respectively to the SGS contribution, the differentiation errors and the aliasing errors.

As expected, the discrete system (10) and the formal model (3) have a similar left-hand sides but the residual terms are different. The inclusion of the discretization into the modeling is responsible for the generation of differentiation and aliasing errors. As pointed out by former studies [6–9,14], this demonstrates that it may be appropriate to make reference to the numerical methods when LES modeling is developed, or at least to design criteria on discretization algorithms ensuring that the numerical errors $R_{\text{fd}}(u)$ and $R_{\text{al}}(u)$ are not the leading terms in (10).

2.2. LES with graded filter

The previous section focused on LES with scale separation implicitly achieved by the projection of the solution on the grid. Graded spatial filters can also be used. Assuming that the filtering operation, denoted $\bar{\cdot}$, commutes with spatial derivatives, it is straightforward to show that the filtered discretized velocity field, $[\bar{u}^\mathcal{L}]_N = [\bar{u}]_N = \bar{u}_N$, is governed by the equation

$$\frac{\partial \bar{u}_N}{\partial t} + \frac{\delta}{\delta X} F_N(\bar{u}_N) = \bar{R}_{\text{sgs}}(u) + \bar{R}_{\text{fd}}(u) + \bar{R}_{\text{al}}(u) \tag{14}$$

with the residual terms:

$$\bar{R}_{\text{sgs}}(u) = \frac{\delta}{\delta X} [F(\bar{u})^\mathcal{L} - \overline{F(u)}]_N, \tag{15}$$

$$\bar{R}_{\text{fd}}(u) = \frac{\delta}{\delta X} [\overline{F(u)}]_N - \left[\frac{\partial}{\partial X} \overline{F(u)} \right]_N, \tag{16}$$

$$\bar{R}_{\text{al}}(u) = \frac{\delta}{\delta X} [F(\bar{u})^\mathcal{L}]_N. \tag{17}$$

As pointed out for instance by Lund and Kaltenbach [15], it is worth noting that filtering may be used to reduce numerical errors. For the finite-differencing errors, if the poorly resolved scales, that are those for which there are large discrepancies between $\delta/\delta x$ and $\partial/\partial x$, are removed by the filter, the differentiation errors $\bar{R}_{\text{fd}}(u)$ tend to vanish.

3. Two-point stochastic closure for numerical error analysis of LES

In the following sections the classical EDQNM model, referred to as EDQNM-DNS [7], is presented. In addition, an EDQNM-LES model is proposed in order to estimate the evolution of the kinetic energy spectrum deduced from a large-eddy simulation with given numerical methods.

3.1. The eddy-damped quasi-normal Markovian approach

In this section, the derivation of the analytical models of turbulence relying on the eddy-damped quasi-normal Markovian (EDQNM) approach is shortly described. An extensive overview of the EDQNM theory may be found in Lesieur [16].

Consider an homogeneous isotropic incompressible turbulence. For a wavenumber k the Navier–Stokes equations in the Fourier space can schematically be written as

$$\left(\frac{\partial}{\partial t} + \nu k^2 \right) u = uu, \tag{18}$$

where ν is the viscosity and u the velocity field. Starting from (18) and introducing the ensemble averaging $\langle \cdot \rangle$, a series of equations can be derived for the velocity correlations. In particular, the double and triple correlations are governed by

$$\left(\frac{\partial}{\partial t} + 2\nu k^2\right)\langle uu \rangle = \langle uuu \rangle, \quad (19)$$

$$\left[\frac{\partial}{\partial t} + \nu(k^2 + p^2 + q^2)\right]\langle uuu \rangle = \langle uuuu \rangle. \quad (20)$$

Eq. (19) is of particular interest since it can be used to determine the evolution of the kinetic energy spectrum $E(k, t)$. However, as shown by (20), the triple correlations $\langle uuu \rangle$ are unclosed terms which need to be modeled.

For a velocity field close to a Gaussian state, namely using a quasi-normal approximation, the 4th-order moments $\langle uuuu \rangle$ can be expressed as functions of the double correlations $\langle uu \rangle$. To ensure realizability of the kinetic energy spectrum, eddy-damping is furthermore introduced. Expression (20) hence reads

$$\left[\frac{\partial}{\partial t} + \nu(k^2 + p^2 + q^2)\right]\langle uuu \rangle = \sum \langle uu \rangle \langle uu \rangle - (\mu_k + \mu_p + \mu_q)\langle uuu \rangle, \quad (21)$$

where μ_k is the eddy-damping rate for a wavenumber k . The solution of this differential equation is easily deduced by means of time integration:

$$\langle uuu \rangle(t) = \int_0^t \sum \langle uu \rangle \langle uu \rangle e^{-\Omega_{kpq}t} dt \quad (22)$$

with $\Omega_{kpq} = \mu_k + \mu_p + \mu_q + \nu k^2 + \nu p^2 + \nu q^2$. The process of Markovianization then enables to further simplify this term. Assuming that the time scale of the 2nd-order moments $\langle uu \rangle$ is large compared to that of the eddy-damping, one can eventually evaluate the 3rd-order moments as

$$\langle uuu \rangle(t) = \Theta(t) \sum \langle uu \rangle \langle uu \rangle, \quad (23)$$

where $\Theta(t)$ is a relaxation time. The time evolution of the kinetic energy spectrum is then computed by introducing the above closure into (19).

3.2. EDQNM-DNS model

The model is referred in this work to EDQNM-DNS to avoid any confusion with the EDQNM-LES framework defined in the next section.

For a freely decaying homogeneous isotropic incompressible turbulence, the time evolution of the kinetic energy spectrum $E(k)$ at a wavenumber k can be written as

$$\left(\frac{\partial}{\partial t} + 2\nu k^2\right)E(k) = T(k), \quad (24)$$

where time dependence of the spectrum is implicit and ν stands for the viscosity [16]. The energy transfers due to triadic interactions read as

$$T(k) = \int \int_{\Delta_k} S(k, p, q) dp dq, \quad (25)$$

whose integrand $S(k, p, q)$ is given by

$$S(k, p, q) = \Theta_{kpq}(t) \frac{E(q)}{q} (xy + z^3)(k^2 E(p) - p^2 E(k)). \quad (26)$$

The geometrical coefficients x , y and z are introduced using the following relationships:

$$x = -\frac{p_i q_i}{pq}, \quad y = -\frac{k_i q_i}{kq}, \quad z = -\frac{p_i k_i}{pk}. \quad (27)$$

The integration domain Δ_k , shown in Fig. 1(a), is such as

$$\Delta_k = \{(p, q) | k + q \geq p \geq |k - q|\} = \{(p, q) | |z| \leq 1\}. \quad (28)$$

Finally, the triple correlation relaxation time is provided by

$$\Theta_{kpq}(t) = \frac{1 - \exp[-\mu_{kpq}t - \nu(k^2 + p^2 + q^2)t]}{\mu_{kpq} + \nu(k^2 + p^2 + q^2)} \quad (29)$$

with $\mu_{kpq} = \mu_k + \mu_p + \mu_q$. The eddy-damping rate μ_k is related to the kinetic energy spectrum using the model proposed by Lesieur [16]

$$\mu_k = 0.19 C_\eta^{3/2} \left[\int_0^k k'^2 E(k') dk' \right]^{1/2}, \quad (30)$$

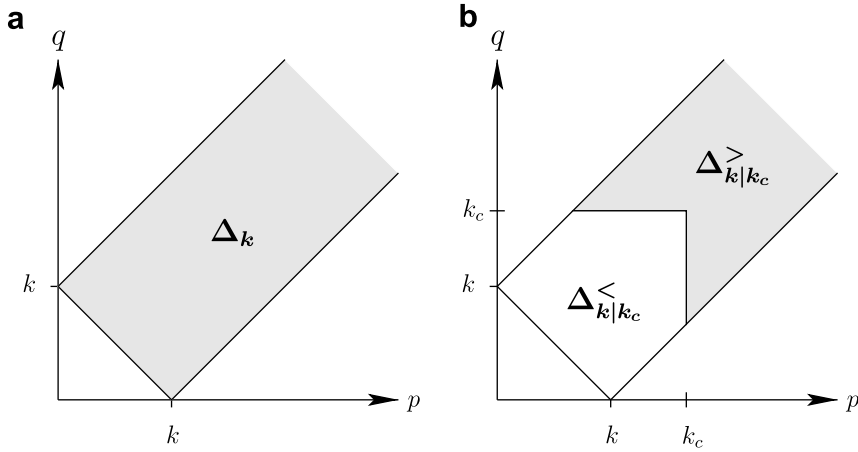


Fig. 1. Sketch in the (p, q) -plane of the integration domains used to compute the nonlinear transfers for the EDQNM-DNS calculations. (a) Full domain, and (b) separation into a resolved and a non-resolved domain given a cut-off wavenumber k_c .

where the Kolmogorov constant C_η is taken to be equal to 1.4 as in Chollet and Lesieur [17].

For practical resolution of the governing equation (24) a logarithmic wavenumber mesh is designed as

$$k_i = k_{\min} 2^{(i-1)/F} \quad \text{for } i = 1, \dots, N, \tag{31}$$

where k_{\min} is the minimum wavenumber of the mesh, F the number of points per decade and N the total number of points. The integral in (24) giving the energy transfer due to nonlinear interactions is approximated using the algorithm introduced by Leith [18]. The corrective term introduced by Lesieur [16] is implemented in order to take into account non-local triadic couplings which are poorly resolved by Leith’s scheme. Adding this term is necessary since the present calculations aim in particular at evaluating SGS energy transfers. Time integration is performed using the Euler method with a time step determined using the criterion $\Delta t < 1/(vk_N^2)$.

The initial spectrum contains most of its energy at small wavenumbers and is prescribed as in [19] by

$$E(k) = 16 \sqrt{\frac{2}{\pi}} \frac{v_0^2}{k_0} \left(\frac{k}{k_0}\right)^4 \exp\left[-2\left(\frac{k}{k_0}\right)^2\right]. \tag{32}$$

The maximum of energy occurs for the wavenumber k_0 , and the velocity v_0 is related to the total kinetic energy Q_{ke} by $Q_{ke} \simeq (3/2)v_0^2$.

The value of the viscosity ν is set to obtain a given gap between the energy-containing scales and the Kolmogorov scale once the initial spectrum (32) has evolved towards a turbulent state. The number of points N of the computation is chosen so that the Kolmogorov scale remains within the wavenumber mesh.

The Reynolds number is evaluated using the Taylor scale λ as $Re_\lambda = \lambda v_0/\nu$ and the dimensionless time is defined by $t^* = k_0 v_0 t$.

3.3. EDQNM-LES model

Consider the large-eddy simulation of a freely decaying homogeneous isotropic turbulence with a cut-off wavenumber k_c , and with scale separation implicitly achieved by the projection of the velocity field on the mesh. The derivation of the EDQNM-DNS model describing the numerical implementation of the LES and the explicit formulations of the various quantities introduced in this section are provided in Appendix A. The time evolution of the truncated kinetic energy spectrum E^* of the LES velocity field is given by

$$\left(\frac{\partial}{\partial t} + 2\nu_i k^2 + 2\nu\chi_k^2 k^2\right)E^*(k) = T_{nl}(k) + T_{al}(k), \tag{33}$$

where $T_{nl}(k)$ corresponds to the energy transfers due to triadic interactions between resolved scales, and $T_{al}(k)$ takes into account aliasing effects occurring when nonlinear terms are discretized. Approximate differentiation is characterized by the isotropic ratio χ_k between the norm of the modified wavenumber and the exact wavenumber. SGS modeling is performed in an artificial manner: an eddy-viscosity based SGS model is introduced by imposing a non-zero turbulent viscosity $\nu_i(k)$ defined in the spectral space. The numerical implementation of the model is nonetheless not considered. Numerical errors and SGS modeling are therefore decoupled and the impact of the discretization can be singly investigated. One may refer to the works of Park and Mahesh [7] for an EDQNM-LES approach involving the practical implementation of a dynamic Smagorinsky model [20].

The numerical resolution of the integro-differential system (33) relies on the same numerical methods as those used for the classical EDQNM-DNS calculations, described in Section 3.2.

3.4. Static error analysis

3.4.1. Resolved and non-resolved energy transfers

Consider the EDQNM-DNS model. Following a SGS modeling point of view, a truncation at some wavenumber k_c is introduced into Eq. (24):

$$\left(\frac{\partial}{\partial t} + 2\nu k^2\right)E(k) = T^<(k|k_c) + T^>(k|k_c), \quad (34)$$

where it is assumed that $k < k_c$. The contribution $T^<(k|k_c)$ from the resolved scales corresponds to the triadic interactions (k, p, q) such as p and q are lower than k_c . The non-resolved transfers $T^>(k|k_c)$ involving triads (k, p, q) with p or q greater than the cut-off wavenumber k_c . The SGS contribution is hence provided by $T^>(k|k_c)$.

The explicit formulations of the resolved and non-resolved energy transfers are obtained by decomposing the full integration domain Δ_k in (25) into a set of resolved wavenumbers $\Delta_{k|k_c}^<$ and a set of non-resolved wavenumbers $\Delta_{k|k_c}^>$ defined by

$$\Delta_{k|k_c}^> = \{(p, q) \in \Delta_k | p > k_c \text{ or } q > k_c\} \quad (35)$$

and $\Delta_{k|k_c}^< = \Delta_k \setminus \Delta_{k|k_c}^>$, so that

$$T^<(k|k_c) = \int \int_{\Delta_{k|k_c}^<} S(k, p, q) dp dq, \quad (36)$$

$$T^>(k|k_c) = \int \int_{\Delta_{k|k_c}^>} S(k, p, q) dp dq. \quad (37)$$

Fig. 1(b) shows a sketch of the domains $\Delta_{k|k_c}^>$ and $\Delta_{k|k_c}^<$.

The amplitude of the SGS transfers $T^>(k|k_c)$ will be used in the present investigation as a reference magnitude for the assessment of the numerical errors [6]. Subgrid modeling in practical situations indeed aims at reproducing the effects of the unresolved scales. Therefore, when numerical errors are higher than the magnitude of $T^>(k|k_c)$, the discretization methods can be considered as inappropriate.

3.4.2. Numerical error definitions

Numerical errors are defined by comparing the EDQNM-LES model (34) to the EDQNM-DNS formulation (24). Following the work of Ghosal [6], a static error analysis is performed by assuming that the LES provides the exact kinetic energy spectrum ($E^*(k) = E(k)$ for $k < k_c$). The errors are thus deduced from a direct comparison between the exact and the LES spectra. Alternative approaches may have been implemented: the approximate differentiation can be considered as an implicit filtering operation as in Salvetti and Beux [21], or the numerical methods can be included into the SGS stress tensor [22]. In the present work, direct comparison is retained in order to uncouple the issues related to the SGS tensor and those associated with the numerics.

The difference (34) – (24) between the two governing equations should then remain equal to zero, so that

$$\underbrace{T_{\text{nl}}(k) - T^<(k|k_c) - 2\nu k^2[E(k) - \chi_k^2 E^*(k)]}_{\text{differentiation}} + \underbrace{T_{\text{al}}(k)}_{\text{aliasing}} + \underbrace{2\nu_t k^2 E^*(k) - T^>(k|k_c)}_{\text{s.g.s}} = 0. \quad (38)$$

Numerical errors are hence defined as the magnitude of the above terms. The following quantities are then introduced:

$$\mathcal{E}_{\text{fd}}(k) = |T_{\text{nl}}(k) - T^<(k|k_c)| + |2\nu k^2[E(k) - \chi_k^2 E^*(k)]|, \quad (39)$$

$$\mathcal{E}_{\text{al}}(k) = |T_{\text{al}}(k)|, \quad (40)$$

$$\mathcal{M}_{\text{sgs}}(k) = |T^>(k|k_c)|. \quad (41)$$

The differentiation error $\mathcal{E}_{\text{fd}}(k)$ evaluates the inaccuracies due to the approximate differentiation algorithm. It compares in particular the difference between the approximate evaluation of the triadic interactions within the mesh and the exact energy transfers $T^<(k|k_c)$ due to the resolved scales. The aliasing errors $\mathcal{E}_{\text{al}}(k)$ provide the magnitude of the aliasing effects. Finally, the amplitude $\mathcal{M}_{\text{sgs}}(k)$ of the subgrid scales contribution deduced from the EDQNM-DNS is used in this work as an acceptable upper bound for the numerical errors [6].

3.4.3. Detailed scale contribution to the errors

Considering the error definitions provided in Section 3.4.2, it is interesting to determine which scales are mainly responsible for the numerical errors.

Let $\mathcal{E}(k)$ be the spectrum of a numerical error of the form

$$\mathcal{E}(k) = \int \int_{\Delta_k} s(k, p, q) dp dq, \quad (42)$$

where $s(k, p, q)$ is the integrand. In the calculation of $\mathcal{E}(k)$, one can restrict the domain of integration to wavenumbers smaller than a given wavenumber k' . This can be done by replacing the quadrature domain Δ_k in (42) by $\Delta_{k|k'}^<$ so that a new quantity $\mathcal{E}^*(k, k')$ is obtained, with

$$\mathcal{E}^*(k, k') = \int \int_{\Delta_{k|k'}^<} s(k, p, q) dp dq. \tag{43}$$

Taking the derivative with respect to k' then yields

$$\zeta(k, k') = \frac{\partial}{\partial k'} [\mathcal{E}^*(k, k')]. \tag{44}$$

This quantity $\zeta(k, k')$, referred to as the detailed scale contribution, estimates the net effect on the error $\mathcal{E}(k)$ when scales with wavenumbers between k' and $k' + dk'$ are taken into account in the integral (42).

3.5. Dynamic error analysis

An alternative to the error definitions proposed in Section 3.4.2 has been proposed by Park and Mahesh [7] in order to assess the global impact of the numerics on the solution. The contribution of approximate differentiation is for instance defined by

$$\sigma_{fd}(t) = \frac{\int_0^{k_c} |E^*(k, t) - E_{fd-}^*(k, t)| dk}{\int_0^{k_c} E^*(k, t) dk}, \tag{45}$$

where $E_{fd-}^*(k, t)$ corresponds to the spectrum provided by the EDQNM-LES model given by Eq. (33) but using spectral methods with $\chi_k = 1$. Similarly, the aliasing contribution $\sigma_{al}(t)$ is calculated using the spectrum $E_{al-}^*(k, t)$ obtained when the aliasing energy transfers $T_{al}(k)$ are set to zero. Finally, the contribution from the SGS model is denoted by $\sigma_{sgs}(t)$ and is evaluated using the spectrum $E_{sgs-}^*(k, t)$ provided by the EDQNM-LES model when the spectral eddy viscosity model is “turned off”, i.e. $\nu_t(k) = 0$ for all k .

4. Results

4.1. Reference solutions (EDQNM-DNS)

4.1.1. Run parameters

The EDQNM-DNS parameters are presented in Table 1. Three calculations have been performed with Reynolds number Re_λ equal to 780, 2500 and 8000.

The EDQNM-DNS calculations have been carried out up to $t^* = 20$ and the results are evaluated once the decay of the kinetic energy spectrum has become self-similar. In this section, self-similar decay is assumed to be reached when the eddy turnover time Q_{ke}/ϵ (ϵ is the dissipation) increases as a power of law with time [16]. The results are therefore provided at $t^* = 8$ when the decay criterion is fulfilled for all the computations.

This behaviour is illustrated in Fig. 2 where the kinetic energy spectra obtained for $Re_\lambda = 2500$ at time t^* equal to 0, 1, 2 and 8 are plotted as a function of the wavenumber k . Starting at $t^* = 0$ from an energy repartition mainly clustered on small wavenumbers, the kinetic energy spectral density $E(k)$ then progressively converges towards a turbulent spectrum with a well-defined inertial range extending up to the dissipative scales.

4.1.2. Evolved spectra

Evolved kinetic spectra deduced from the EDQNM-DNS calculations at $t^* = 8$ are plotted in Fig. 3 for $Re_\lambda = 780, 2500, 8000$. The three spectra exhibit typical features of decaying homogeneous isotropic turbulence: a k^4 slope for large scales, an inertial range with a decay close to $k^{-5/3}$ and a severe decrease of the spectral density in the neighborhood of the Kolmogorov scale. As expected, the larger the Reynolds number, the wider the gap between the energy-containing scales and the dissipative scales.

4.1.3. Subgrid scale contribution

As mentioned above, the SGS energy transfers are of special interest in this study. To assess their relevancy, the contributions $T^>(k|k_c)$ obtained from the residual motions deduced from the EDQNM-DNS are recast in term of the normalized spectral eddy viscosity [17] defined by

Table 1
Run parameters of the EDQNM calculations

Re_λ	ν	F	N
780	10^{-4}	8	145
2500	10^{-5}	8	165
8000	10^{-6}	8	185

For all the computations the following quantities remain unchanged: $k_{min} = 1/32, k_0 = 1$ and $\nu_0 = 1$. The Reynolds number Re_λ is evaluated at $t^* = 8$.

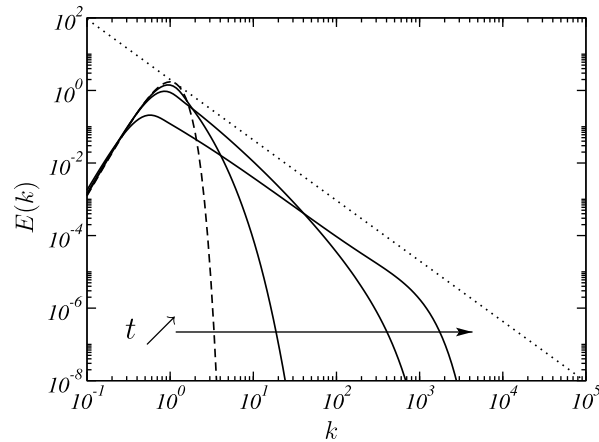


Fig. 2. Time evolution of the kinetic energy spectrum $E(k)$ provided by the EDQNM-DNS calculations, as a function of the wavenumber k , for $Re_\lambda = 2500$. ---, $E(k, t^* = 0)$; —, $E(k, t^*)$ for $t^* = 1, 2, 8$; ·····, $E(k) \propto k^{-5/3}$.

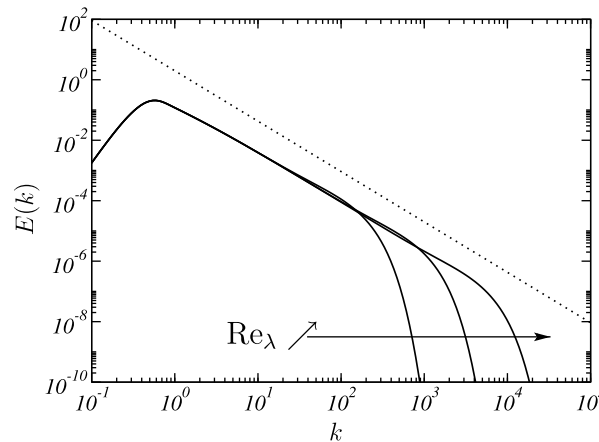


Fig. 3. Evolved kinetic energy spectra at $t^* = 8$ provided by the EDQNM-DNS calculations for $Re_\lambda = 780, 2500, 8000$. —, $E(k, t^* = 8)$; ·····, $E(k) \propto k^{-5/3}$.

$$v_t^+(k/k_c) = \frac{T^>(k/k_c)}{-2k^2 E(k)} \sqrt{\frac{k_c}{E(k_c)}} \quad (46)$$

and is compared to the fitting function

$$v_t^+(k/k_c) = 0.441 C_\eta^{-3/2} \left[1 + 34.467 \exp\left(-3.03 \frac{k_c}{k}\right) \right] \quad (47)$$

proposed by Chollet [23].

The normalized spectral eddy viscosity at $t^* = 8$ is presented in Fig. 4 for the calculation with $Re_\lambda = 2500$ as a function of the wavenumber k/k_c for various cut-off wavenumbers ($k_c = 4, 8, 16, 32$). The fitting function (47) is also plotted for comparison. The EDQNM-DNS and theoretical eddy viscosities are in good agreement, independently of the cut-off wavenumber. A typical plateau-cusp shape is visible: when resolved and non-resolved turbulence scales are well separated, the eddy viscosity is constant, whereas local interactions across the boundary $k = k_c$ are responsible for the cusp close to the cut-off [24].

Similar results are obtained for the calculations with Reynolds numbers $Re_\lambda = 780$ and $Re_\lambda = 2500$.

4.2. EDQNM-LES

4.2.1. Run parameters

The EDQNM-LES calculations are performed using the parameters of the EDQNM-DNS. Three Reynolds numbers 780, 2500 and 8000 are considered with cut-off wavenumbers k_c equal to 4, 8, 16 and 32. The approximate derivatives are carried out by standard finite differences of order ranging from 2 to 14.

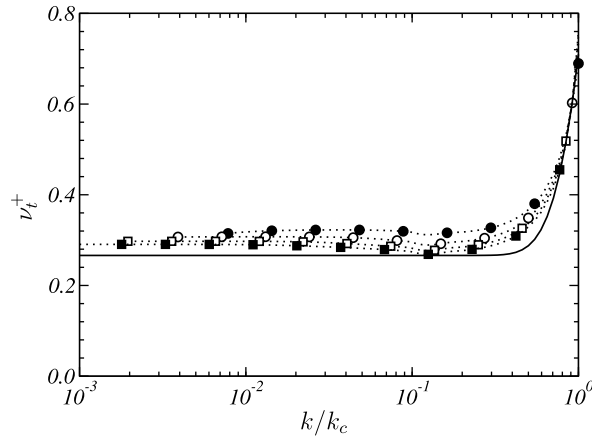


Fig. 4. Normalized spectral eddy viscosity v_t^+ as a function of the wavenumber k normalized by the cut-off wavenumber k_c , provided by the EDQNM-DNS calculations for $Re_\lambda = 2500$. —, fitting function of Chollet [23]; ...••••, $k_c = 4$; ...○•••, $k_c = 8$; ...□•••, $k_c = 16$; ...■•••, $k_c = 32$.

To avoid any discussion about numerical errors during the transient evolution of the spectrum, the EDQNM-LES computations are initialized at $t^* = 8$ with the spectra deduced from the EDQNM-DNS and truncated at the cut-off wavenumber k_c .

4.2.2. Ideal LES – pure physical LES

An ideal LES is first considered to provide a reference of a pure physical LES, where inaccuracies are only due to modeling errors. An EDQNM-LES calculation is then performed using spectral methods with $\chi_k = 1$. In addition, the aliasing contribution $T_{al}(k)$ in Eq. (33) is artificially set to zero. The spectral eddy viscosity v_t is deduced from the fitting function of Chollet [23] given by Eq. (47) so that

$$v_t(k) = v_t^+(k/k_c) \sqrt{\frac{E^*(k_c)}{k_c}}, \tag{48}$$

where k_c is the LES wavenumber cut-off wavenumber.

The kinetic energy spectrum obtained at $t^* = 16$ for $Re_\lambda = 2500$ and $k_c = 32$ with the ideal LES is plotted against the wavenumber in Fig. 5. A very good collapse is observed between the EDQNM-LES results and the reference data for all the resolved scales.

4.2.3. Practical LES – numerical errors

The practical implementation of LES often involves discretization tools with limited order of accuracy such as finite differences. Spectral methods indeed lack of generality because proper orthogonal bases are only available for few simple flow geometries.

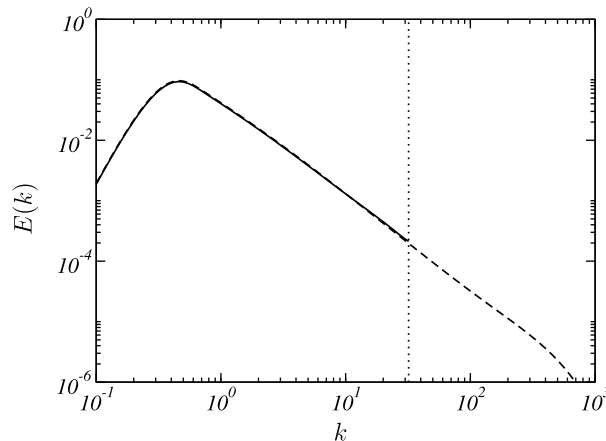


Fig. 5. Evolved kinetic energy spectra at $t^* = 16$ provided by the EDQNM-LES calculation for $Re_\lambda = 2500$ and $k_c = 32$, for an ideal LES (spectral methods and $T_{al}(k)$ is set to zero). —, $E(k, t^* = 16)$; ---, reference solution at $t^* = 16$ provided by the EDQNM-DNS model. (The dotted line stands for the LES cut-off.)

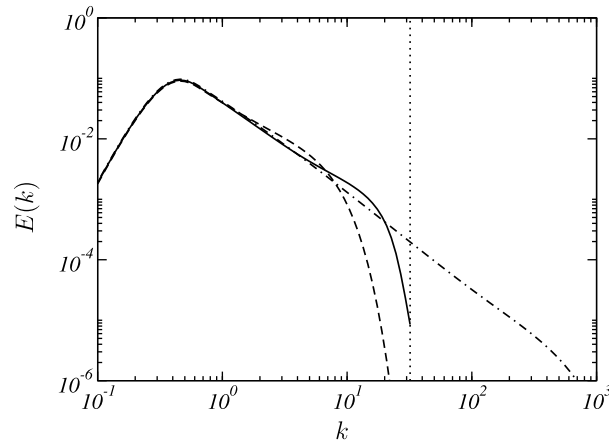


Fig. 6. Evolved kinetic energy spectra at $t^* = 16$ provided by the EDQNM-LES calculation for $Re_\lambda = 2500$ and $k_c = 32$, for 2nd-order and 10th-order approximate derivatives, with spectral eddy viscosity. ---, 2nd-order scheme; —, 10th-order scheme; -·-·-, EDQNM-DNS reference solution. (The dotted line stands for the LES cut-off.)

Approximate differentiation operators unfortunately generate numerical errors. This point is illustrated in Fig. 6 where the evolved kinetic energy spectra obtained with the EDQNM-LES model (33), using the spectral eddy viscosity (48), are plotted at $t^* = 16$, for $Re_\lambda = 2500$ and $k_c = 32$. The results obtained using the 2nd- and 10th-order finite differences, as well as the reference spectrum of the EDQNM-DNS calculation, are presented.

Discrepancies between the EDQNM-LES and the reference spectra are clearly visible for both orders of accuracy of the finite differences. The wavenumbers close to the mesh cut-off are particularly poorly resolved with strong underestimations of the kinetic energy. The larger scales appear to be better calculated. The inaccuracies previously observed are related to the aliasing errors and to the limited bandwidth of the numerical methods which cannot resolve all the scales supported by the mesh.

As an example, the aliasing and differentiation errors obtained for the 10th-order finite-difference scheme are plotted in Fig. 7 as functions of the wavenumber, for $k_c = 32$ and $Re_\lambda = 2500$. The magnitude of the SGS contribution $|T^>(k|k_c)|$ is also provided for comparison. It must be remarked that numerical errors have a cumulative effect since localized errors in the spectrum progressively contaminate all the resolved scales due to nonlinearities. To avoid any discussion on this point, the numerical errors are evaluated at the beginning of the runs, i.e. at $t^* = 8$. Considering Fig. 7, one can first observe that the aliasing error is small compared to the differentiation error and to the SGS contribution. The weak influence of the aliasing on the solution was formerly pointed out by Park and Mahesh [7]. On the contrary, the differentiation error exhibits large values, which are in particular higher than the SGS contributions for small scales in the neighborhood of the grid cut-off. For $0.02 < k/k_c < 0.3$, the differentiation error does not vary appreciably and is lower than the SGS contribution. For larger scales, characterized by $k/k_c < 0.02$, the differentiation error and the SGS contribution display finally close values. Similar trends are observed for the other finite-difference schemes, especially regarding the low magnitude of the aliasing errors. The study will therefore now focus on the differentiation errors.

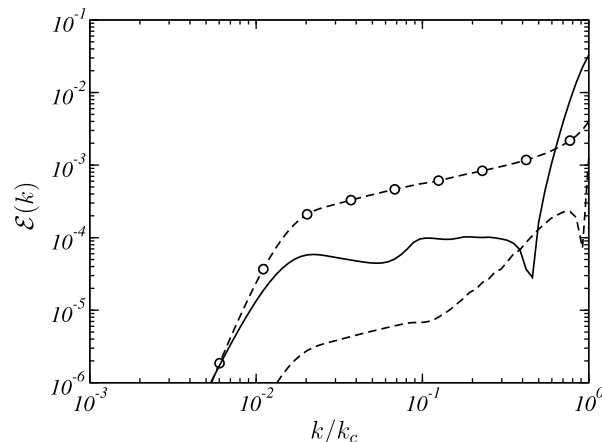


Fig. 7. Differentiation error $\varepsilon_{fd}(k)$ and aliasing error $\varepsilon_{al}(k)$ at $t^* = 8$ as functions of the wavenumber k normalized by the cut-off wavenumber k_c , provided by the EDQNM-LES calculations for $Re_\lambda = 2500$ and $k_c = 32$, with approximate differentiation of order 10. —, $\varepsilon_{fd}(k)$; ---, $\varepsilon_{al}(k)$; -○-, magnitude of the subgrid scale contribution $|T^>(k|k_c)|$.

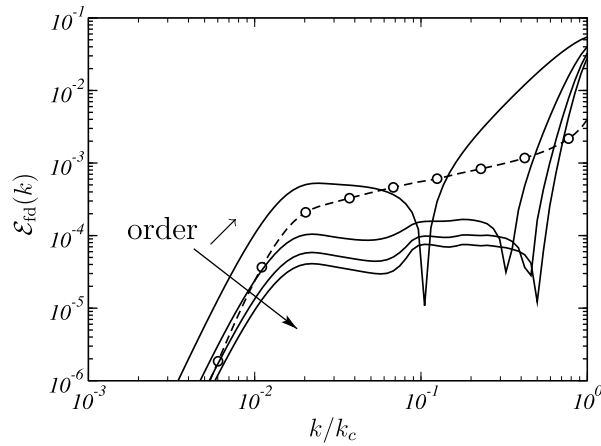


Fig. 8. Differentiation error $\mathcal{E}_{fd}(k)$ as a function of the wavenumber k/k_c for $Re_z = 2500$ and for $k_c = 32$, at $t^* = 8$. Approximate differentiation of order 2, 6, 10 and 14. —, $\mathcal{E}_{fd}(k)$; -○-, magnitude of the subgrid scale contribution $|T^>(k|k_c)|$.

4.3. Static error analysis

4.3.1. Order of accuracy

The differentiation error $\mathcal{E}_{fd}(k)$ is first presented in Fig. 8, where it is plotted against the normalized wavenumber k/k_c for approximate derivatives of order 2, 6, 10 and 14. The results are calculated at the beginning of the run ($t^* = 8$) with $Re_z = 2500$ and $k_c = 32$. The modulus of the SGS contribution $|T^>(k|k_c)|$ is also represented and used as an acceptable upper bound. The error curves are found to exhibit similar shapes with large amplitudes close to the grid cut-off wavenumber, a plateau approximately centered on $k/k_c = 10^{-1}$ and a decrease in k^5 as the wavenumber tends to zero. The emergence, for all the schemes, of this k^5 slope as $k \rightarrow 0$ is discussed in Appendix B by means of an asymptotic development of the differentiation errors.

One can furthermore observe that increasing the order of accuracy of the discretization method reduces the numerical errors. The 2nd-order scheme indeed yields large differentiation errors, higher than the SGS energy transfer for most of the wavenumbers supported by the mesh. The differentiation errors are significantly smaller with schemes of higher order. Using the 14th-order scheme for instance, the numerical errors are negligible for all wavenumbers except for those close to the mesh cut-off wavenumber.

It must be however noted that increasing the order of accuracy mainly acts on LES accuracy at high wavenumbers. Indeed when the formal order increased in Fig. 8, the k^5 slope as $k \rightarrow 0$ and the plateau level are weakly modified whereas the wavenumber range where differentiation errors are large is severely narrowed. This result is interesting since one could have expected the formal order to be related to the accuracy at the larger scales.

The relationships between numerical errors and the properties of the approximate differentiation can be interpreted by studying the detailed scale contribution to the numerical errors. The detailed scale contribution $\zeta_{fd}(k, k')$ to the differentiation error $\mathcal{E}_{fd}(k)$ is plotted as a function of k'/k_c in Fig. 9(a) and (b) for $k = 1$ and $k = 4$, respectively. The results are evaluated at $t^* = 8$, for $Re_z = 2500$ and $k_c = 32$, and algorithms of order 2, 6, 10 and 14 are considered. For $k = 1$ and for the 2nd-order scheme, the detailed scale contribution shows a maximum in the neighborhood of $k' = k$, corresponding here to $k'/k_c \simeq 0.03$. The contribution $\zeta_{fd}(k, k')$ is then seen to slowly decrease when k' tends to the grid cut-off wavenumber k_c . A large range of wavenumbers therefore contributes to the error. When the formal order of the differentiation algorithm is increased, a significant decrease of the contributions from the larger scales is observed. At $k'/k_c \simeq 0.03$, there is for instance about six orders of magnitude between the contributions obtained with the 2nd- and the 6th-order schemes. On the other hand, the contributions from the scales close to the mesh cut-off wavenumber appear to be weakly influenced by the order of accuracy, as shown by the similar amplitude of $\zeta_{fd}(k, k')$ in the neighborhood of $k' = k_c$, for all the algorithms. This generation of differentiation errors from the high wavenumbers could be explained by the gap between the exact and the approximate differentiations close to the mesh cut-off wavenumber. Indeed, even though long range interactions between the reference wavenumber $k = 1$ and the wavelengths close to the cut-off wavenumber with $k' \sim k_c$ are likely to involve few energy transfers, the inability of the algorithms to resolve these high wavenumbers still produces significant numerical errors. It can be noticed that, according to Fig. 9(a), small scales contribution dominates the numerical errors for schemes of order equal or higher than 4.

The same conclusions hold for the reference wavenumber $k = 4$ in Fig. 9(b). The contribution from the larger scales ($k'/k_c \sim 0.1$) is seen to decrease with the order of accuracy, whereas $\zeta_{fd}(k, k')$ exhibits high values in the neighborhood of the mesh cut-off wavenumber for all the schemes.

4.3.2. Order of accuracy versus modified wavenumber optimization

Increasing the formal order of a discretization scheme is the simplest technique to improve the accuracy of the numerical method. Larger stencil sizes must however be used and the computational cost is increased. Scheme optimization in the Fou-

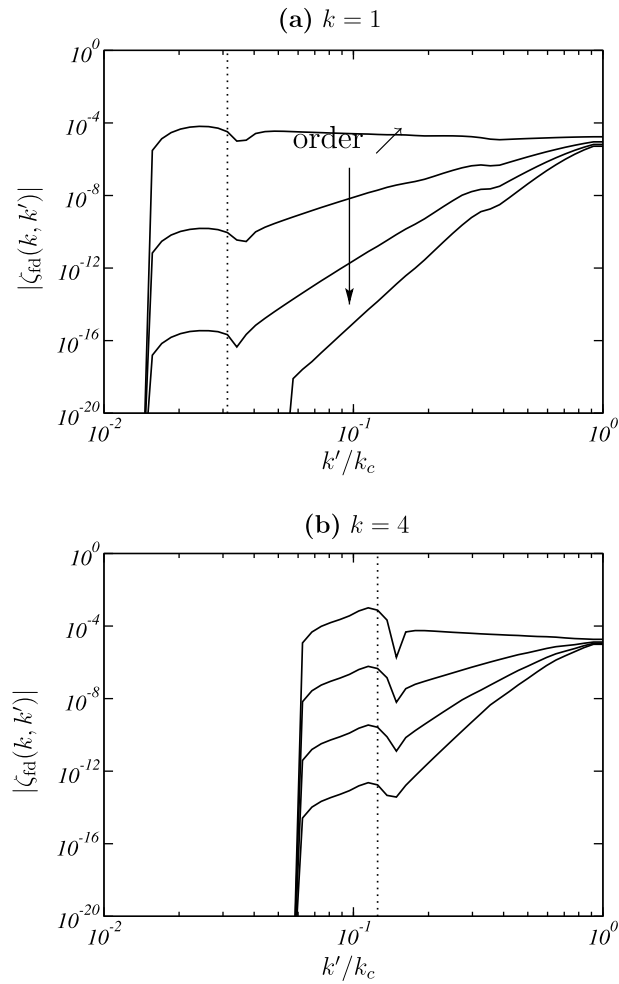


Fig. 9. Detailed scale contribution $|\zeta_{fd}(k, k')$ to the differentiation errors $\mathcal{E}_{fd}(k)$ as a function of the wavenumber k'/k_c for $Re_\lambda = 2500$ and $k_c = 32$, and for various reference wavenumbers k , at $t^* = 8$. Approximate differentiation of order 2, 6, 10 and 14. —, $|\zeta_{fd}(k, k')$. Reference wavenumbers. The dotted line indicates where the reference wavenumber is located on the axis k'/k_c .

rier space [5] is an alternative technique allowing to increase the resolution range of approximate derivatives while keeping constant the number of points of the algorithm. The formal order is then reduced in order to freely determine some coefficients of the scheme which can be determined by optimizing the modified wavenumber in the spectral space. The accuracy at low wavenumbers is lowered but higher wavenumbers, especially those close to the grid cut-off, are better resolved. According to the investigation of the detailed scale contribution $\zeta_{fd}(k, k')$ carried out in the previous section, the optimized schemes are of special interest since the EDQNM-LES showed that most of the numerical errors are generated by the smallest scales resolved by the mesh.

The differentiation error $\mathcal{E}_{fd}(k)$ is plotted in Fig. 10 as a function of k/k_c for the 4th-order 11-point and 4th-order 13-point optimized finite differences designed by Bogey and Bailly [11]. The error for the standard 10th-order scheme is also presented for comparison. The Reynolds number is $Re_\lambda = 2500$ and the mesh cut-off $k_c = 32$. Compared to the 10th standard scheme, the 11-point optimized algorithm provides lower numerical errors. It is worth noting that due to its higher accuracy at high wavenumbers, the 11-point optimized scheme results in an error reduction for all the wavenumbers under consideration, including the larger scales with $k/k_c < 10^{-2}$. In a similar manner, the 4th-order 13-point optimized algorithm yields low differentiation errors over a large interval of wavenumbers. In particular in this case, the range of badly calculated wavenumbers close to the mesh cut-off is $0.7 < k/k_c < 1$, which is quite narrow.

4.3.3. Accuracy limit and efficiency rate

The spectrum of the differentiation errors can be used to estimate an accuracy limit for each scheme. In the present work an arbitrary criterion based on the amplitude of the numerical errors is introduced. The accuracy limit k_a is defined as the smallest wavenumber so that $\mathcal{E}_{fd}(k_a) > 10^{-3}$. It is evaluated here for $Re_\lambda = 2500$ and for a grid cut-off wavenumber equal to $k_c = 32$.

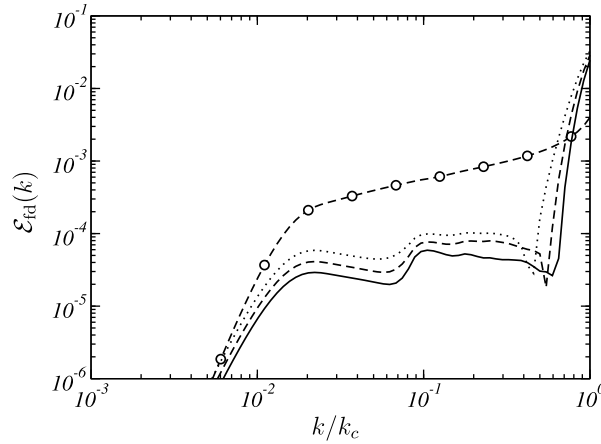


Fig. 10. Differentiation error $\mathcal{E}_{fd}(k)$ as a function of the wavenumber k/k_c for $Re_\lambda = 2500$ and for $k_c = 32$, at $t^* = 8$. $\dots\dots\dots$, 10th standard finite differences; $-\dots-$, 11-point optimized scheme [11]; $-\dots-$, 13-point optimized scheme [11]; $-\circ-$, magnitude of the subgrid scale contribution $|T^\infty(k/k_c)|$.

In addition, in order to take into account the computational effort required to achieve a given accuracy, the definition of an efficiency rate e_a is proposed with

$$e_a = \frac{1}{(2N_s + 1)(k_c/k_a)^3}, \tag{49}$$

where $(2N_s + 1)$ corresponds to the number of points of the scheme, and $(k_c/k_a)^3$ represents the increase in grid nodes to improve the accuracy from k_a to k_c for a 3D simulation. The rate e_a is then related to the inverse of the number of operations that would be necessary to shift the accuracy limit from k_a to k_c . Therefore, the higher value of e_a , the more efficient the discretization method.

The accuracy limits k_a/k_c and the efficiency rates are respectively presented in Fig. 11(a) and (b) as functions of the number of points $(2N_s + 1)$ of the schemes, for standard and optimized finite differences. Standard schemes of order up to 20 are considered. For these schemes, as expected, the accuracy limit monotonically grows with the stencil size and ranges from $k_a/k_c = 0.15$ for the 2nd-order scheme, to $k_a/k_c = 0.7$ for the 20th-order algorithm. An increase of k_a is furthermore observed for the optimized schemes compared to the standard schemes with the same number of points.

Consider now the efficiency rate e_a in Fig. 11(b). For the standard schemes, the rate e_a first becomes higher with the number of points of the scheme, reaches a maximum for the 13- and 15-point algorithms and then slowly decreases for higher order schemes. Therefore, when schemes with larger stencil size are used, the gain in accuracy is higher than the increase in computational cost for $2N_s + 1 \leq 15$, which is no longer the case for $2N_s + 1 > 15$. Fig. 11(b) nevertheless shows that the efficiency can be increased thanks to scheme optimization in the Fourier space. The 11- and 13-point optimized schemes indeed exhibit the highest efficiency rates. Compared to the standard schemes with the same number of points, the efficiency rate is doubled for the 11-point and 13-point optimized algorithms.

4.3.4. Reynolds number

The influence of the Reynolds number on the differentiation errors is now investigated. The differentiation error $\mathcal{E}_{fd}(k)$ is represented as a function of k/k_c for the standard algorithm of order 10 in Fig. 12 for the Reynolds numbers $Re_\lambda = 780$, $Re_\lambda = 2500$ and $Re_\lambda = 8000$. The grid cut-off wavenumber is taken to be $k_c = 32$. The differentiation errors estimated for the different Reynolds numbers are found to collapse very well. Similar results are obtained with the other schemes. The differentiation errors therefore do not appreciably depend on the Reynolds number.

4.3.5. Grid convergence

The grid convergence is investigated in Fig. 13 where the differentiation error $\mathcal{E}_{fd}(k)$ is plotted against the wavenumber k , for the grid cut-off wavenumbers $k_c = 32$, $k_c = 16$ and $k_c = 8$. The Reynolds number is $Re_\lambda = 2500$ and the 10th-order scheme is considered. For the three cases, the differentiation error exhibits a similar shape: a k^5 slope for the larger scales, then a plateau, and the curves finally reach large values for wavenumbers close to the mesh cut-off wavenumber. Furthermore the overall magnitude of the differentiation error appears weakly influenced by the grid refinement. It turns out that the major effect of the grid refinement is to shift the maximum of differentiation error towards smaller scales. The magnitude of the numerical errors then shows little reduction for small wavenumbers $k/k_c < 0.5$. According to Fig. 13, grid convergence in LES is hence not ensured since refining the grid does not guarantee the reduction of the numerical errors for the smaller wavenumbers. As pointed out in Section 4.3.1 where the detailed scale contribution $\zeta_{fd}(k, k')$ to the differentiation error

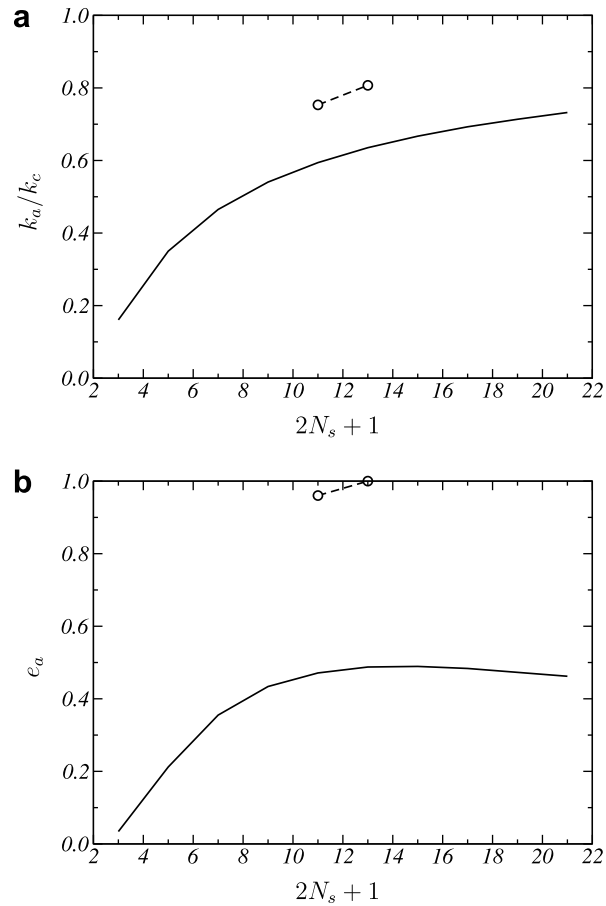


Fig. 11. (a) Accuracy limit k_a/k_c and (b) efficiency rate e_a of the standard and optimized finite differences as functions of the number of points $2N_s + 1$ of the algorithms. Results obtained at $Re_\tau = 2500$ with a grid cut-off $k_c = 32$. —, standard schemes; -○-, optimized schemes. Note that efficiency rates are normalized by the efficiency rate of the 13-point optimized scheme of Bogey and Bailly [11].

$\mathcal{E}_{fd}(k)$ is studied, the scales close to the grid cut-off have a major contribution to the numerical errors. In LES at sufficiently high Reynolds numbers, whatever the mesh size, these high wavenumbers still carry out a non-negligible amount of energy and are therefore responsible for a significant part of the numerical errors.

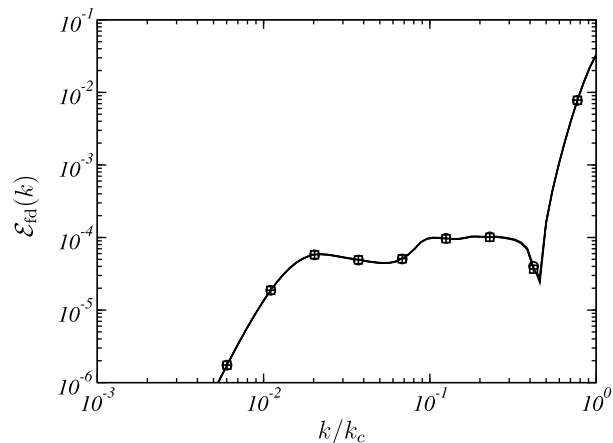


Fig. 12. Differentiation error $\mathcal{E}_{fd}(k)$ as a function of the wavenumber k/k_c for $k_c = 32$, and for various Reynolds number Re_τ , at $t^* = 8$. Approximate differentiation of order 10. —○—, $Re_\tau = 780$; —□—, $Re_\tau = 2500$; —+—, $Re_\tau = 8000$.

4.3.6. LES convergence

The LES convergence is eventually considered. A spectral truncation is hence introduced at some cut-off wavenumber k_f . The cut-off wavenumber of the spectral eddy viscosity model is set to k_f and the differentiation errors are analyzed for vanishing mesh size ($k_c \rightarrow 0$) but at fixed filter width ($k_f = \text{cte}$).

As an example, the differentiation error $\mathcal{E}_{\text{fd}}(k)$ of a 10th-order scheme is first represented in Fig. 14 as a function of the wavenumber k/k_c for $Re_\lambda = 2500$ and at $t^* = 8$. Various mesh cut-off wavenumbers ($k_c = 32, 64, 128, 256$) are considered. The spectral cut-off wavenumber k_f is kept constant equal to 32. The numerical errors are shown to decrease when the mesh size is pushed towards smaller scales. There is for instance about 9 orders of magnitude between the differentiation errors obtained for $k_c = 32$ and $k_c = 256$.

In this situation, when the filter width is kept constant, the rate of decrease of the differentiation errors is indeed linked to the order of accuracy of the algorithm. To demonstrate this assumption the total differentiation error Q_{fd} is evaluated by integrating the differentiation errors $\mathcal{E}_{\text{fd}}(k)$ over the resolved wavenumbers:

$$Q_{\text{fd}} \equiv \int_0^{k_f} \mathcal{E}_{\text{fd}}(k) dk. \tag{50}$$

The total differentiation error Q_{fd} is depicted in Fig. 15 as a function of the grid cut-off wavenumber k_c for differentiation algorithms of order 2, 6, 10 and 14, at $t^* = 8$ and $Re_\lambda = 2500$. For all the schemes, the total error is seen to decrease when the mesh size becomes smaller. The slopes of the error curves are furthermore equal to the order of the algorithms. For instance, a good collapse between the curve $Q_{\text{fd}} \propto k_c^{-10}$ and the total error of the 10th-order scheme is indeed observed when k_c is large enough. The same conclusion holds for the other schemes.

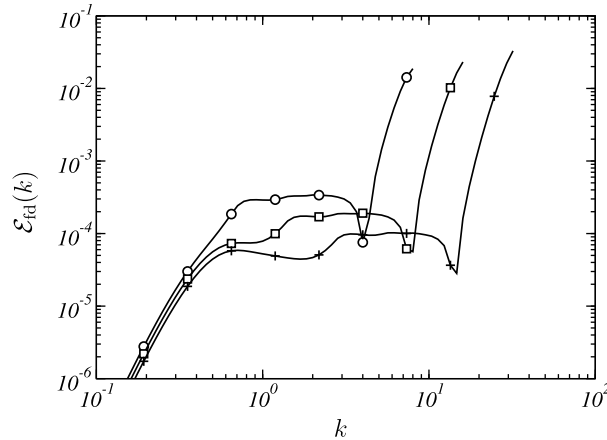


Fig. 13. Differentiation error $\mathcal{E}_{\text{fd}}(k)$ as a function of the wavenumber k/k_c for $Re_\lambda = 2500$ and for various mesh cut-off k_c , at $t^* = 8$. Approximate differentiation of order 10. —○—, $k_c = 8$; —□—, $k_c = 16$; —+—, $k_c = 32$.

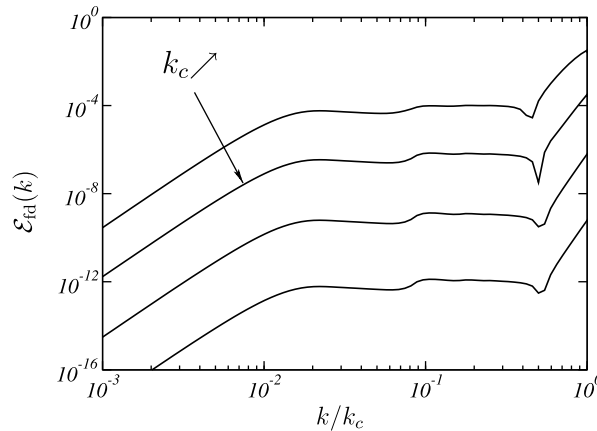


Fig. 14. Differentiation error $\mathcal{E}_{\text{fd}}(k)$ as a function of the wavenumber k/k_c for $Re_\lambda = 2500$ and for various mesh cut-off wavenumber ($k_c = 32, 64, 128, 256$), and with a constant spectral cut-off wavenumber $k_f = 32$, at $t^* = 8$. Approximate differentiation of order 10.

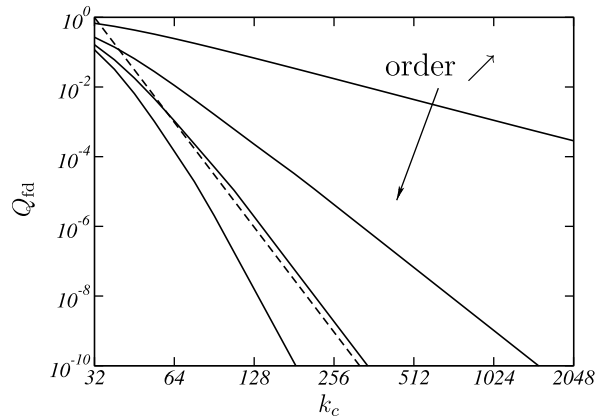


Fig. 15. Total differentiation error Q_{fid} as a function of the grid cut-off wavenumber k_c , for a constant cut-off wavenumber $k_f = 32$, at $t^* = 8$ with $Re_\lambda = 2500$. Approximate differentiation of order 2, 6, 10 and 14 are represented. —, Q_{fid} ; ---, $Q_{\text{fid}} \propto k_c^{-10}$.

We may thus conclude that LES convergence (i.e. when the mesh size goes to zero with the filter width size is kept constant) occurs. The convergence is moreover directly related to the order of accuracy of the approximate differentiation scheme.

4.3.7. Explicit filtering

Practical discretization tools thus introduce numerical errors over a more or less wider range of wavenumbers depending on the order of accuracy. Even though low accuracy only occurs for some wavenumbers, it may be appropriate to remove these wavenumbers. The energy redistribution by the triadic interactions within the resolved scales can indeed lead to a contamination of the full spectrum by the numerical errors.

Filtering of the flow variables at a cut-off wavenumber k_f smaller than the grid cut-off wavenumber k_c can reduce inaccuracy spreading within resolved scales [6,15]. This approach is furthermore used, and has been discussed by several research groups [25–28]. Flux filtering [22,30] can be implemented with the same aim in view but will be not considered in the present work. It has been however for instance shown that such a filtering might generate specific dispersion errors in the Fourier space [29] that should be taken into account in the assessment of LES based on flux filtering.

Explicit filtering is now briefly illustrated using spectral filters with a cut-off wavenumber that is smaller than the accuracy limit k_a of the differentiation algorithm. In the framework of the EDQNM-LES model, spectral filtering is equivalent to setting the kinetic energy spectrum to zero for $k > k_f$, at each time step. Note that in this case the cut-off wavenumber in the spectral eddy viscosity model (48) is equal to the filter cut-off wavenumber with

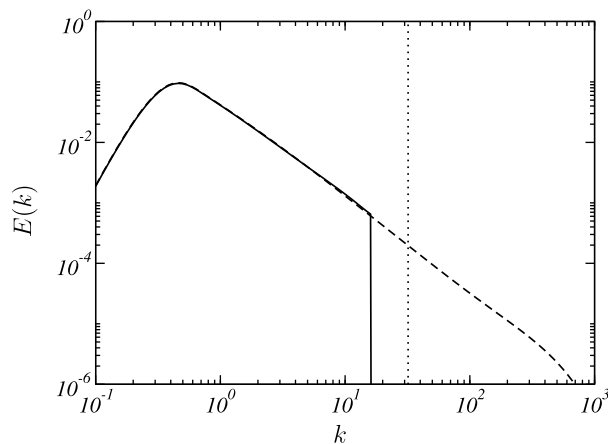


Fig. 16. Evolved kinetic energy spectra at $t^* = 16$ provided by the EDQNM-LES calculation for $Re_\lambda = 2500$ and $k_c = 32$, for 10th-order approximate derivatives, with spectral explicit filtering at $k_f = k_c/2$ and with spectral eddy viscosity. —, 10th-order finite differences; ---, EDQNM-DNS reference solution. (The dotted line stands for the LES cut-off.)

$$v_t(k) = v_t^+(k/k_f) \sqrt{\frac{E(k_f)}{k_f}} \tag{51}$$

The accuracy improvement using filtering is illustrated by performing an EDQNM-LES run for the 10th-order finite differences at $Re_\lambda = 2500$, with the spectral eddy viscosity model and a filter-size-to-grid-width ratio such as $k_c/k_f = 2$. Waves discretized by less than 4 points per wavelength are then removed from the calculation. Fig. 16 shows the kinetic energy spectrum obtained at $t^* = 16$ with the EDQNM-LES model and the reference spectrum of the EDQNM-DNS. A good agreement is observed over the whole range of resolved wavenumbers. The improvement of the resolution is especially visible when this spectrum is compared to the spectrum of Fig. 6 which is obtained without filtering and shows larger discrepancies.

It should be nonetheless remarked that the use of explicit filtering shifts the effective LES cut-off towards larger scales. The overall SGS contribution is consequently seen to increase and larger modeling errors may be observed in practical situations.

4.4. Dynamic error analysis

The influence of the SGS model, approximate differentiation and aliasing is now investigated using the contributions $\sigma_{fd}(t)$, $\sigma_{al}(t)$ and $\sigma_{sgs}(t)$ defined in Section 3.5. In what follows, the aliasing contribution will be not discussed since its magnitude has been found to be very low for all the LES configurations considered in the present work.

The SGS contribution $\sigma_{sgs}(t)$ and the approximate differentiation contribution $\sigma_{fd}(t)$ are plotted as functions of time t^* in Fig. 17(a)–(d) for standard algorithms of order 2, 6, 10 and 14, respectively. The Reynolds number is $Re_\lambda = 2500$ and the LES cut-off wavenumber is set to $k_c = 32$. It turns out that for all the order of accuracy, the differentiation errors clearly overwhelm the influence of the SGS model. For example, for the 2nd-order algorithm at $t^* = 16$, there is more than three orders of magnitude between the SGS contribution and the approximate differentiation contribution. Comparison between Fig.

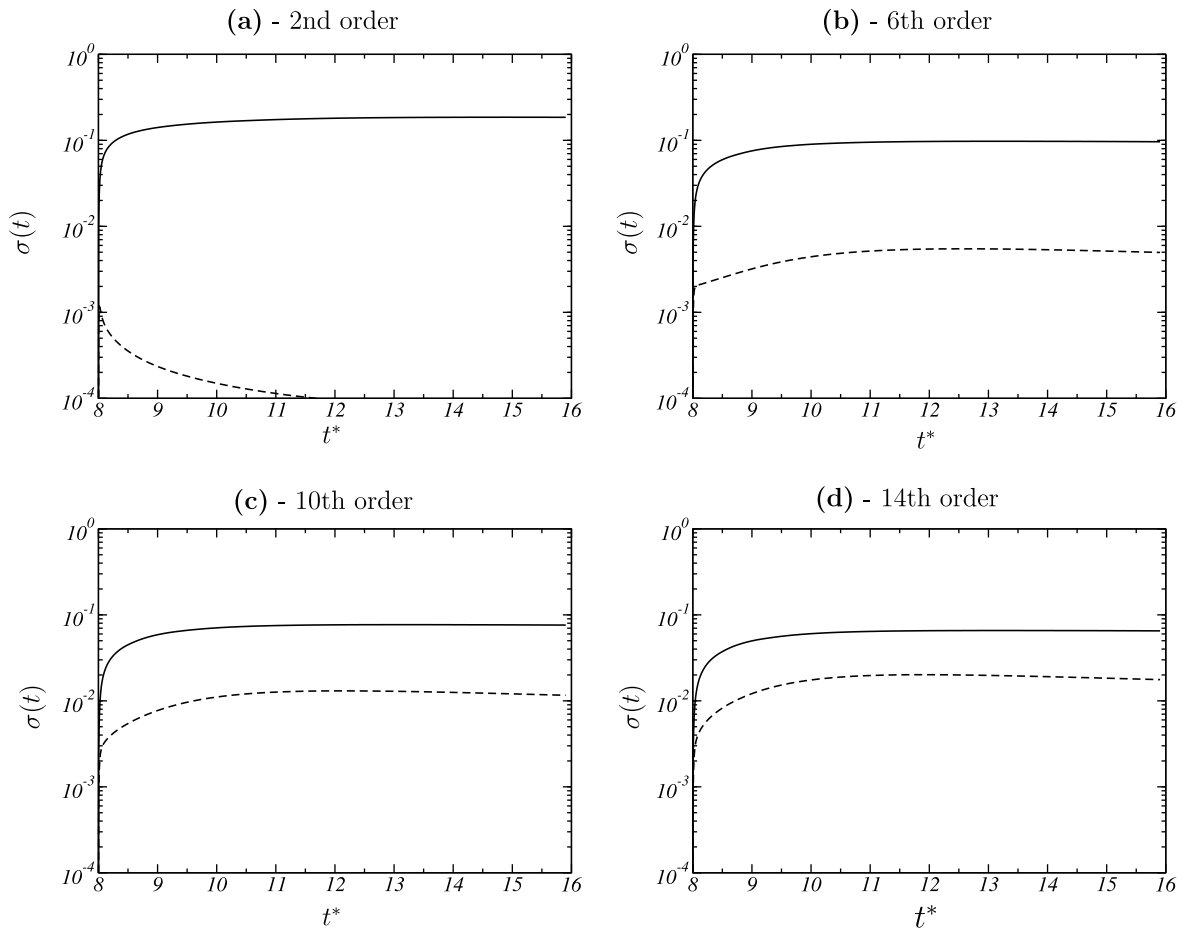


Fig. 17. Temporal evolution of the contributions of the SGS model, of the approximate differentiation and of the aliasing provided by the EDQNM-LES calculation for $Re_\lambda = 2500$ and $k_c = 32$, for approximate differentiation of order 2, 6, 10 and 14. ---, $\sigma_{sgs}(t)$; —, $\sigma_{fd}(t)$.

17(a)–(d) shows that the gap between the SGS and the approximate differentiation contributions may be reduced using higher-order schemes. Nevertheless, numerical errors are still larger than the SGS contribution by a factor of four for the 14th-order scheme, at $t^* = 16$.

These observations tend to demonstrate that approximate differentiation has a major impact on a the solution, whatever the order of accuracy of the algorithm may be. Note however that the previous test case is somehow not relevant. Indeed, according to the definition of the spectral eddy viscosity $\nu_\tau(k)$ provided by Eq. (48) the amplitude of the SGS term is given by $E^*(k_c)$. The model is therefore particularly sensitive to the quality of the solution around $k = k_c$. As shown for instance in Fig. 16, the EDQNM-LES strongly underestimates the magnitude of the kinetic energy spectrum at the grid cut-off wavenumber. To propose more reliable results, the contributions are also evaluated using a spectral eddy viscosity whose amplitude is given by

$$\nu_\tau(k) = \nu_\tau^+(k/k_c) \sqrt{\frac{E_c}{k_c}}. \quad (52)$$

The parameter E_c is deduced from the EDQNM-DNS reference data, with $E_c = E(k_c)$ so that the amplitude of the SGS term is ensured to be correct.

The contributions of the correct SGS model deduced from (52) and of the approximate differentiation for $Re_\lambda = 2500$ and $k_c = 32$ are provided in Fig. 18(a)–(d) as functions of the time t^* , for standard algorithms of order 2, 6, 10 and 14, respectively. Numerical errors still appear to have a significant influence on the solution quality since the approximate differentiation contribution $\sigma_{\text{al}}(t)$ remains larger or close to the SGS contribution $\sigma_{\text{al}}(t)$ for all the algorithms. Nevertheless, using the correct SGS model, the gap between the SGS and the differentiation contributions is seen to decrease when the order of accuracy increases. For the 14th-order algorithm, the SGS contribution $\sigma_{\text{al}}(t)$ is even the largest contribution for $t^* > 10$. One may therefore expect that numerical errors will be easier to curb when high-order filters are implemented.

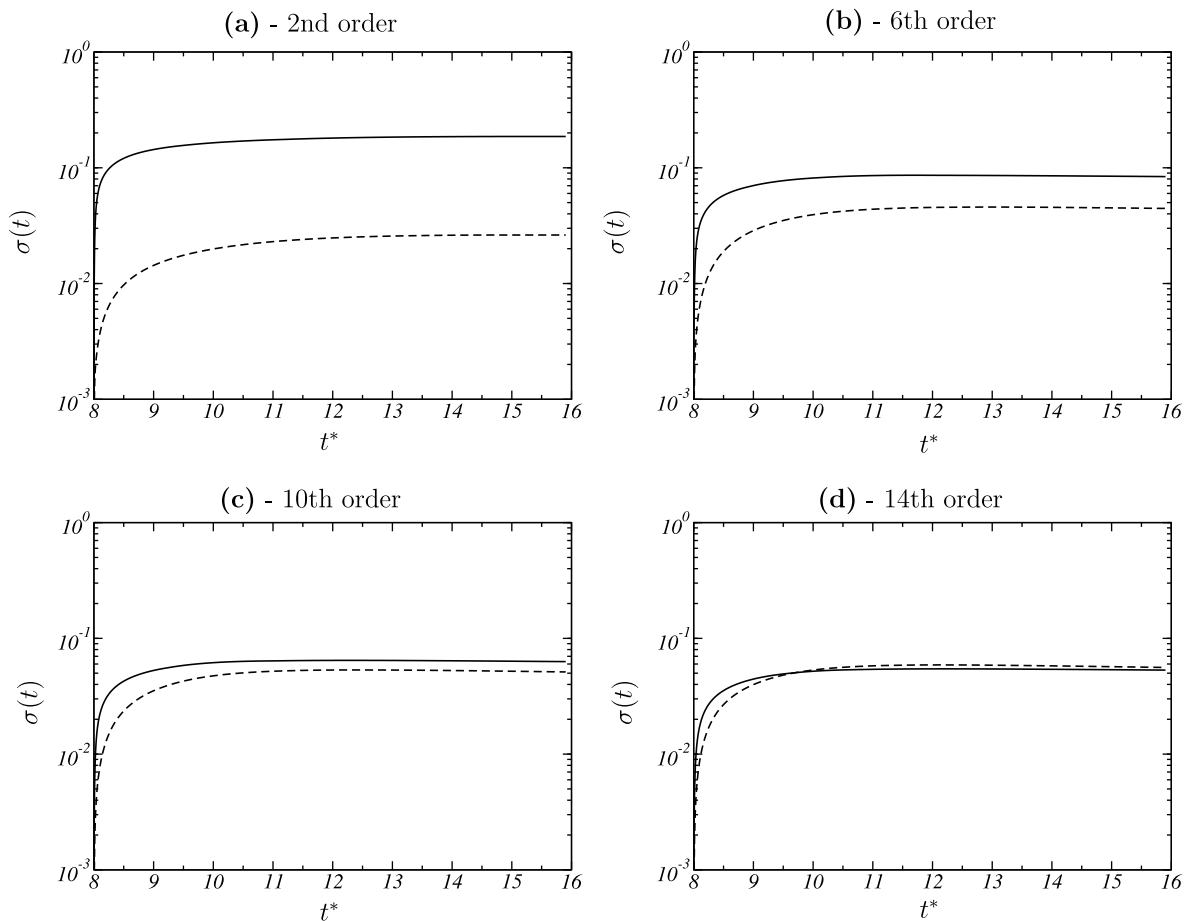


Fig. 18. Temporal evolution of the contributions of the SGS model (with an amplitude deduced from DNS data) and of the approximate differentiation provided by the EDQNM-LES calculation for $Re_\lambda = 2500$ and $k_c = 32$, for approximate differentiation of order 2, 6, 10 and 14. ---, $\sigma_{\text{sgs}}(t)$; —, $\sigma_{\text{al}}(t)$.

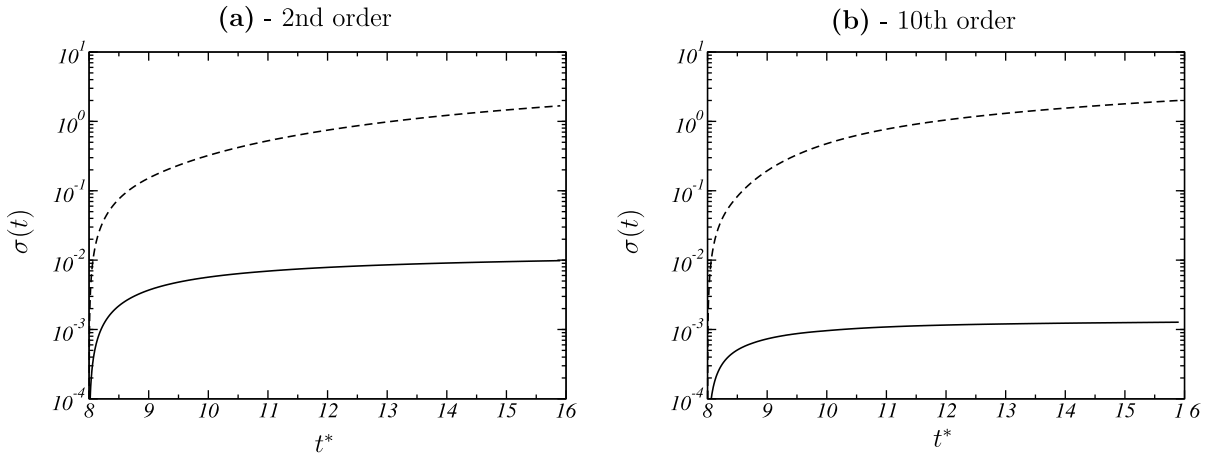


Fig. 19. Temporal evolution of the contributions of the SGS model and of the approximate differentiation provided by the EDQNM-LES calculation for $Re_\lambda = 2500$ and $k_c = 32$. (a) 2nd-order approximate differentiation with spectral explicit filtering at $k_f = k_c/8$ and (b) 10th-order approximate differentiation with spectral explicit filtering at $k_f = k_c/2$. ---, $\sigma_{sgs}(t)$; —, $\sigma_{id}(t)$.

This assumption is further supported when explicit filtering is considered. The SGS and approximate differentiation contributions obtained at $Re_\lambda = 2500$ and $k_c = 32$ are plotted as functions of time t^* in Fig. 19(a) for the 2nd-order algorithm with spectral explicit filtering at $k_f = k_c/8$ and in Fig. 19(b) for the 10th-order algorithm with spectral explicit filtering at $k_f = k_c/2$. The filter cut-off wavenumbers correspond to those prescribed by Ghosal [6]. The SGS contribution is seen to be widely dominant over the whole calculation for both order of accuracy, so that it is ensured that approximate differentiation has negligible impact on the solution quality. There are for instance two orders of magnitude between the contributions $\sigma_{sgs}(t)$ and $\sigma_{id}(t)$ at $t^* = 16$ for the 2nd-order scheme and three orders of magnitude for the 10th-order scheme. Recall however that the filter cut-off wavenumber k_f for the 2nd-order scheme is four times smaller than the one used for the 10th-order algorithm. The high-order scheme thus allows a wider effective spectral resolution and the computational cost is consequently lowered.

5. Conclusion

A parametric study of the influence on numerical errors of the formal order of the discretization methods in LES has been performed. The derivation in the physical space of a formal model for the discretized filtered Navier–Stokes equations first shows that approximate differentiations and aliasing effects generate additional numerical error terms compared to the classical filtered Navier–Stokes equations. To quantify the numerical errors, an EDQNM-LES model has been developed in order to evaluate the time evolution of the kinetic energy spectrum obtained by a LES based on approximate differentiation algorithms of given orders. Based on the works of Ghosal [6], a static error analysis has been carried out: comparisons to the reference spectra provided by a classical fully-resolved EDQNM approach (EDQNM-DNS) allowed us to define and to calculate the differentiation and the aliasing errors for three cases of decaying incompressible homogeneous isotropic turbulence, with Reynolds number Re_λ based on the Taylor scale equal to 780, 2500 and 8000, for differentiation methods of order 2 to 14, and for optimized algorithms [11]. Following Park and Mahesh [7], contributions of the SGS model, approximate differentiation and aliasing have been defined with the aim of performing a dynamic error analysis.

The aliasing errors are first observed to be very small. On the contrary, the differentiation errors may dominate the SGS contribution, especially for low-order schemes. Increasing the order of accuracy reduces differentiation errors, but mainly for wavenumbers close to the grid cut-off. The detailed scale contribution to the differentiation errors furthermore shows that the interactions between scales in the neighborhood of the mesh cut-off are responsible for a major part of the numerical errors, even at low wavenumbers. This trend has been confirmed by considering 11- and 13-point optimized finite differences. Compared to the standard schemes, the optimized algorithms resolve short wavelengths in a better way, and lead to a reduction of the differentiation errors has been observed for all wavenumbers. The results have been recast in terms of accuracy limits and efficiency rates in order to take into account the computational cost required by the discretization tools to reach a given accuracy. The accuracy limit is seen to increase using schemes of higher order or optimized in the Fourier space. Regarding the efficiency rates, a balance between accuracy and computational cost is achieved for the 15-point standard finite differences since the efficiency rates of the standard algorithms exhibit a maximum for this scheme. The highest efficiency rates have been however reached by the optimized schemes which doubled the maximum rate of standard algorithms. In addition, the results are shown to be independent of the Reynolds number. Refining the grid has besides a weak influence on the amplitudes of the numerical errors because reducing the mesh size has been observed to mainly shift the maximum of error towards smaller scales. Nonetheless, it turns out that refining the grid while keeping the effective

scale separation at a constant wavenumber using a spectral truncation reduces numerical errors. The rate of convergence is furthermore directly connected to the order of accuracy of the algorithm. Finally, the dynamic error analysis further supports the above conclusions: using high-order schemes leads to lower differentiation errors. Moreover, explicit filtering of the flow solution permits to reduce numerical errors so that the SGS contribution becomes dominant again.

Within the framework of EDQNM-LES, differentiation errors are hence a non-negligible element of the simulation. Using high order or optimized schemes seems to be appropriate since differentiation errors then occur only for a narrow wavenumber band close to the grid cut-off, so that only a small part of the turbulence spectrum is poorly resolved. Nevertheless, due to quadratic interactions between wavenumbers, numerical errors spread, and the whole spectrum can be contaminated. Explicit filtering is then an interesting alternative. The technique has been briefly discussed in this work for spectral filters but a deeper investigation would be needed, especially for the case of discrete filters [11,31].

Appendix A. Derivation of the EDQNM-LES closure

This section aims at deriving an EDQNM model describing the evolution of the numerical implementation of a large-eddy simulation. Note that time dependence of the flow variables (velocities and energy spectrum in particular) has been dropped out for the sake of simplicity.

Consider the LES of a freely decaying incompressible homogeneous isotropic turbulence on an infinite domain with scale separation implicitly achieved by the projection of the velocity field on the mesh. The LES cut-off wavenumber is k_c and the set of wavenumbers that can be represented on the grid is

$$\square = [-k_c, k_c] \times [-k_c, k_c] \times [-k_c, k_c]. \quad (\text{A.1})$$

The resolved velocity field provided by the LES is denoted by $\mathbf{u}_N(\mathbf{x})$ and its Fourier component by $\hat{\mathbf{u}}_N(\mathbf{k}) = (\hat{v}_1(\mathbf{k}), \hat{v}_2(\mathbf{k}), \hat{v}_3(\mathbf{k}))$ for a wavenumber vector $\mathbf{k} = (k_i)$.

A.1. Approximate derivatives

The differentiation algorithm is characterized by its modified wavenumber [5], denoted by $\tilde{\mathbf{k}}$, and defined so that numerical differentiation in the Fourier space is equivalent to a multiplication by $i\tilde{\mathbf{k}}$

$$\widehat{\nabla_N \mathbf{u}_N}(\mathbf{k}) = i\tilde{\mathbf{k}}\mathbf{u}_N(\mathbf{k}), \quad (\text{A.2})$$

where ∇_N is a discrete approximation of the differential operator ∇ . Such a representation is nonetheless not isotropic since the mesh axes define particular directions. The modified wavenumber is therefore made isotropic by means of an average over the sphere of radius $|\mathbf{k}|$ for an arbitrary component of $\tilde{\mathbf{k}}$. More precisely, the quantity χ_k is introduced with

$$\chi_k = \frac{1}{4\pi} \int_{\theta \in [0, 2\pi]} \int_{\varphi \in [0, \pi]} \frac{\tilde{k}_x}{k_x} \sin \varphi \, d\varphi \, d\theta, \quad (\text{A.3})$$

where k_x is an arbitrary component of \mathbf{k} . For instance, for $\alpha = 1$, we have $k_x = k \sin \varphi \cos \theta$. Numerical differentiation is then assumed to only introduce an isotropic bias given by

$$\widehat{\nabla_N \mathbf{u}_N}(\mathbf{k}) = i\chi_k \mathbf{k} \mathbf{u}_N(\mathbf{k}) \quad (\text{A.4})$$

The numerical evaluation of Eq. (A.3) providing the isotropic ratio χ_k is performed using the following algorithm:

$$\chi_k = \frac{1}{4\pi} \sum_{\theta_i, \varphi_j} \frac{\tilde{k}_x}{k_x} \sin \varphi_i \Delta\varphi \Delta\theta \quad (\text{A.5})$$

with

$$\begin{aligned} \theta_i &= (i-1) \frac{\pi}{n_p} \quad \text{for } i = 1, \dots, 2n_p + 1, \\ \varphi_j &= (j-1) \frac{\pi}{n_p} \quad \text{for } j = 1, \dots, n_p + 1 \end{aligned} \quad (\text{A.6})$$

and $\Delta\theta = \Delta\varphi = \pi/n_p$. The procedure however is lacking in accuracy for low wavenumbers, especially for high-order schemes. When k tends to zero, the integration errors in (A.6) indeed exceed the small discrepancies between \tilde{k}_x and k_x . An asymptotic expression is hence used for small wavenumbers. Assuming that the formal order of the differentiation algorithm is preserved by the spherical averaging, one may state that when k is small enough, the isotropic ratio is given by

$$\chi_k = 1 - Ak^\gamma, \quad (\text{A.7})$$

where γ is the formal order of the scheme and A is a scaling constant.

The present study makes use of $n_p = 500$ for calculating Eq. (A.6) and the asymptotic formulation (A.7) is used when $\chi_k - 1$ is smaller than 2×10^{-5} . This technique is illustrated for the 10th-order standard scheme in Fig. A.1 where the isotro-

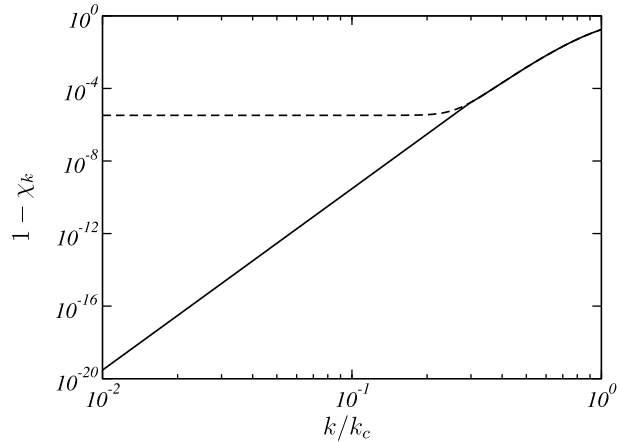


Fig. A.1. Isotropic ratio χ_k between the modified and the exact wavenumber for a 10th-order scheme as a function of k/k_c . —, with asymptotic expression for small wavenumbers; ---, without asymptotic expression.

pic ratio χ_k is plotted against k with and without asymptotic expression for small wavenumbers. The two procedures are found to yield the same ratio χ_k for high wavenumbers. Nevertheless, without asymptotic expression, a plateau due to approximate integration in (A.6) is visible when k tends to zero, and the formal order of the numerical differentiation is not preserved. On the contrary, using an asymptotic development for small wavenumbers provides the expected convergence rate of the isotropic ratio for small wavenumbers. The isotropic ratios obtained for the 2nd-, 6th-, 10th- and 14th-order algorithms are provided in Fig. A.2.

A.2. Numerical LES in the spectral space

Within the theoretical framework introduced by Ghosal [6] the governing equation of the numerical LES reads in the spectral space:

$$\frac{\partial \hat{v}_i}{\partial t}(\mathbf{k}) = \chi_k M_{imn}(\mathbf{k}) \int_{\square^2} \hat{v}_m(\mathbf{p}) \hat{v}_n(\mathbf{q}) \delta_{\mathbf{k}-\mathbf{p}-\mathbf{q}} d\mathbf{p} d\mathbf{q} + \chi_k M_{imn}(\mathbf{k}) \sum_{\mathbf{a} \in \Lambda_0} \int_{\square^2} \hat{v}_m(\mathbf{p}) \hat{v}_n(\mathbf{q}) \delta_{\mathbf{k}-\mathbf{p}-\mathbf{q}-\mathbf{a}} d\mathbf{p} d\mathbf{q} - \nu \chi_k^2 k^2 \hat{v}_i(\mathbf{k}), \tag{A.8}$$

where $\delta_{\mathbf{k}}$ is the Dirac function and Λ_0 is the set of aliasing modes of the grid [6]

$$\Lambda_0 = \{\mathbf{a} | \mathbf{a} = (2pk_c, 2qk_c, 2rk_c) \text{ with } (p, q, r) \in \{-1; 0; 1\}^3, \text{ and } (p, q, r) \neq (0, 0, 0)\}. \tag{A.9}$$

In addition, the projection operators are provided by the relationships

$$M_{imn}(\mathbf{k}) = -iP_{imn}(\mathbf{k}), \tag{A.10}$$

$$P_{imn}(\mathbf{k}) = (k_n P_{im} + k_m P_{in})/2, \tag{A.11}$$

$$P_{ij} = \delta_{ij} - k_i k_j / k^2. \tag{A.12}$$

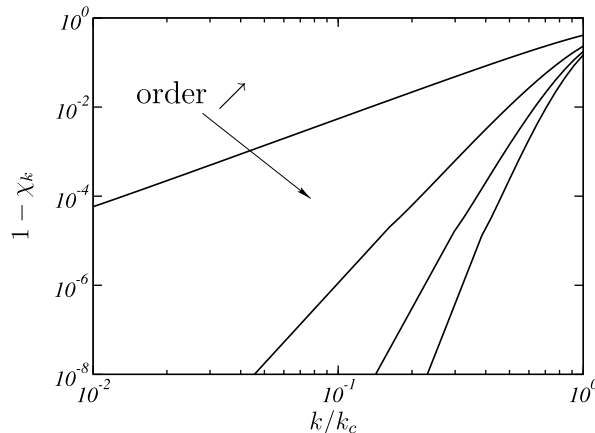


Fig. A.2. Isotropic ratios χ_k between the modified and the exact wavenumber for approximate differentiation of order 2, 6, 10 and 14 as functions of k/k_c .

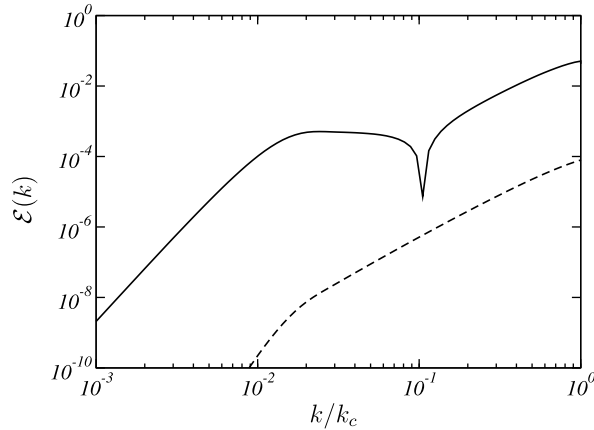


Fig. A.3. Finite-differencing errors due to the nonlinear and the viscous terms for a 2nd-order scheme as a function of k/k_c , for $k_c = 32$ and $Re_\lambda = 2500$. —, nonlinear terms; ---, viscous terms.

Remark that the discretization of the viscous term in (A.8) involves 2nd-order derivative which is modeled by a double application of a first derivative ($\chi_k^2 k^2$). As shown by Park and Mahesh [7] this point can be questionable for low Reynolds number ($Re_\lambda = 70$) turbulent field. The present work however focuses on high Reynolds homogeneous isotropic turbulence with $Re_\lambda > 700$. The finite-differencing errors due to the viscous terms is then several order of magnitudes smaller than the finite-differencing errors due to the nonlinear terms. This trend is illustrated in Fig. A.3 where the finite-differencing errors due to the nonlinear terms, $|T_{nl}(k) - T^c(k|k_c)|$ in Eq. (39), is compared to finite-differencing errors due to the viscous terms, namely $|2\nu k^2[E(k) - \chi_k^2 E^*(k)]|$, for $k_c = 32$ and $Re_\lambda = 2500$. A large difference between differentiation errors associated with nonlinear and viscous terms is observed over the whole range of wavenumbers. Finite-differencing errors due to viscous terms are thus a negligible component of numerical errors and their modelization in the EDQNM-LES framework is not crucial.

A.3. Two-point stochastic closure

Multiplying the LES governing equation (A.8) by $\hat{v}_i(-\mathbf{k})$ and taking the ensemble average $\langle \cdot \rangle$ yields the relationship describing the evolution of the double velocity correlations for the resolved field:

$$\begin{aligned} \left[\frac{\partial}{\partial t} + 2\nu\chi_k^2 k^2 \right] \langle \hat{v}_i(\mathbf{k})\hat{v}_i(-\mathbf{k}) \rangle &= 2\chi_k M_{imn}(\mathbf{k}) \int_{\square^2} \langle \hat{v}_m(\mathbf{p})\hat{v}_n(\mathbf{q})\hat{v}_i(-\mathbf{k}) \rangle \delta_{\mathbf{k}-\mathbf{p}-\mathbf{q}} \mathbf{p} \mathbf{d} \mathbf{q} \\ &+ 2\chi_k M_{imn}(\mathbf{k}) \sum_{\mathbf{a} \in \mathcal{A}_0} \int_{\square^2} \langle \hat{v}_m(\mathbf{p})\hat{v}_n(\mathbf{q})\hat{v}_i(-\mathbf{k}) \rangle \delta_{\mathbf{k}-\mathbf{p}-\mathbf{q}-\mathbf{a}} \mathbf{p} \mathbf{d} \mathbf{q}. \end{aligned} \quad (\text{A.13})$$

The kinetic energy spectrum of the LES resolved velocity field is introduced using

$$E^*(k) = 2\pi k^2 \langle \hat{v}_i(\mathbf{k})\hat{v}_i(-\mathbf{k}) \rangle. \quad (\text{A.14})$$

This spectrum is truncated at the mesh cut-off k_c , with $E^*(k) = 0$ for $k > k_c$. Summing over indices i of the velocity components in the previous equation leads to the kinetic energy equation

$$\begin{aligned} \left[\frac{\partial}{\partial t} + 2\nu\chi_k^2 k^2 \right] E^*(k) &= 4\pi k^2 \chi_k M_{imn}(\mathbf{k}) \int_{\square^2} \langle \hat{v}_m(\mathbf{p})\hat{v}_n(\mathbf{q})\hat{v}_i(-\mathbf{k}) \rangle \delta_{\mathbf{k}-\mathbf{p}-\mathbf{q}} \mathbf{p} \mathbf{d} \mathbf{q} \\ &+ \left\{ 4\pi k^2 \chi_k M_{imn}(\mathbf{k}) \sum_{\mathbf{a} \in \mathcal{A}_0} \int_{\square^2} \langle \hat{v}_m(\mathbf{p})\hat{v}_n(\mathbf{q})\hat{v}_i(-\mathbf{k}) \rangle \delta_{\mathbf{k}-\mathbf{p}-\mathbf{q}-\mathbf{a}} \mathbf{p} \mathbf{d} \mathbf{q} \right\}_{S_k}. \end{aligned} \quad (\text{A.15})$$

It should be noted that isotropy is ensured by replacing the cubic domain of integration \square by a spherical one \circ defined by

$$\circ = \{\mathbf{k} | |\mathbf{k}| \leq k_c\}. \quad (\text{A.16})$$

In addition, the aliasing terms are averaged over the sphere of radius k . The operation is denoted $\{\cdot\}_{S_k}$.

The equation on the triple velocity correlations is obtained by multiplying (A.8) by the appropriate velocity components, taking the ensemble average and summing. We are finally left with

$$\begin{aligned}
 & \left[\frac{\partial}{\partial t} + v(\chi_k^2 k^2 + \chi_p^2 p^2 + \chi_q^2 q^2) \right] \langle \hat{v}_i(-\mathbf{k}) \hat{v}_m(\mathbf{p}) \hat{v}_n(\mathbf{q}) \rangle = \chi_k M_{iab}(-\mathbf{k}) \int_{\mathcal{O}^2} \langle \hat{v}_a(\mathbf{r}) \hat{v}_b(\mathbf{s}) \hat{v}_m(\mathbf{p}) \hat{v}_n(\mathbf{q}) \rangle \delta_{-\mathbf{k}-\mathbf{r}-\mathbf{s}} \mathbf{d}\mathbf{r} \mathbf{d}\mathbf{s} \\
 & + \left\{ \chi_k M_{iab}(-\mathbf{k}) \sum_{\mathbf{a} \in \mathcal{A}_0} \int_{\mathcal{O}^2} \langle \hat{v}_a(\mathbf{r}) \hat{v}_b(\mathbf{s}) \hat{v}_m(\mathbf{p}) \hat{v}_n(\mathbf{q}) \rangle \delta_{-\mathbf{k}-\mathbf{r}-\mathbf{s}-\mathbf{a}} \mathbf{d}\mathbf{r} \mathbf{d}\mathbf{s} \right\}_{S_k} + \chi_p M_{mab}(\mathbf{p}) \int_{\mathcal{O}^2} \langle \hat{v}_a(\mathbf{r}) \hat{v}_b(\mathbf{s}) \hat{v}_i(-\mathbf{k}) \hat{v}_n(\mathbf{q}) \rangle \delta_{\mathbf{p}-\mathbf{r}-\mathbf{s}} \mathbf{d}\mathbf{r} \mathbf{d}\mathbf{s} \\
 & + \left\{ \chi_p M_{mab}(\mathbf{p}) \sum_{\mathbf{a} \in \mathcal{A}_0} \int_{\mathcal{O}^2} \langle \hat{v}_a(\mathbf{r}) \hat{v}_b(\mathbf{s}) \hat{v}_i(-\mathbf{k}) \hat{v}_n(\mathbf{q}) \rangle \delta_{\mathbf{p}-\mathbf{r}-\mathbf{s}-\mathbf{a}} \mathbf{d}\mathbf{r} \mathbf{d}\mathbf{s} \right\}_{S_k} + \chi_q M_{nab}(\mathbf{q}) \int_{\mathcal{O}^2} \langle \hat{v}_a(\mathbf{r}) \hat{v}_b(\mathbf{s}) \hat{v}_m(\mathbf{p}) \hat{v}_i(-\mathbf{k}) \rangle \delta_{\mathbf{q}-\mathbf{r}-\mathbf{s}} \mathbf{d}\mathbf{r} \mathbf{d}\mathbf{s} \\
 & + \left\{ \chi_q M_{nab}(\mathbf{q}) \sum_{\mathbf{a} \in \mathcal{A}_0} \int_{\mathcal{O}^2} \langle \hat{v}_a(\mathbf{r}) \hat{v}_b(\mathbf{s}) \hat{v}_m(\mathbf{p}) \hat{v}_i(-\mathbf{k}) \rangle \delta_{\mathbf{q}-\mathbf{r}-\mathbf{s}-\mathbf{a}} \mathbf{d}\mathbf{r} \mathbf{d}\mathbf{s} \right\}_{S_k}. \tag{A.17}
 \end{aligned}$$

The hypothesis of a quasi-Gaussian velocity field allows to express the 4th-order moments as functions of the 2nd-order moments following:

$$\langle \hat{v}_m(\mathbf{p}) \hat{v}_n(\mathbf{q}) \hat{v}_a(\mathbf{r}) \hat{v}_b(\mathbf{s}) \rangle = +\delta_{\mathbf{p}+\mathbf{q}} \delta_{\mathbf{r}+\mathbf{s}} \Phi_{mn}^*(\mathbf{q}) \Phi_{ab}^*(\mathbf{s}) + \delta_{\mathbf{p}+\mathbf{r}} \delta_{\mathbf{q}+\mathbf{s}} \Phi_{ma}^*(\mathbf{r}) \Phi_{nb}^*(\mathbf{s}) + \delta_{\mathbf{p}+\mathbf{s}} \delta_{\mathbf{q}+\mathbf{r}} \Phi_{mb}^*(\mathbf{s}) \Phi_{na}^*(\mathbf{r}), \tag{A.18}$$

where $\Phi_{ij}^*(\mathbf{k}) = P_{ij}(\mathbf{k}) E^*(k) / (4\pi k^2)$ is the correlation tensor of the resolved velocity field. Introducing $f(k, p) = 1 / (4\pi k p)^2$ and using the symmetry of the velocity component implied by isotropy, one may write

$$\begin{aligned}
 & \left[\frac{\partial}{\partial t} + v(\chi_k^2 k^2 + \chi_p^2 p^2 + \chi_q^2 q^2) \right] \langle \hat{v}_i(-\mathbf{k}) \hat{v}_m(\mathbf{p}) \hat{v}_n(\mathbf{q}) \rangle = +2\delta_{\mathbf{k}-\mathbf{p}-\mathbf{q}} \{ -\chi_k M_{iab}(\mathbf{k}) P_{ma}(\mathbf{p}) P_{nb}(\mathbf{q}) f(p, q) E^*(p) E^*(q) \\
 & + \chi_p M_{mab}(\mathbf{p}) P_{ia}(\mathbf{k}) P_{nb}(\mathbf{q}) f(k, q) E^*(k) E^*(q) + \chi_q M_{nab}(\mathbf{q}) P_{ma}(\mathbf{p}) P_{ib}(\mathbf{k}) f(k, p) E^*(k) E^*(p) \} \\
 & + \left\{ 2 \sum_{\mathbf{a} \in \mathcal{A}_0} \delta_{\mathbf{k}-\mathbf{p}-\mathbf{q}-\mathbf{a}} \{ -\chi_k M_{iab}(\mathbf{k}) P_{ma}(\mathbf{p}) P_{nb}(\mathbf{q}) f(p, q) E^*(p) E^*(q) + \chi_p M_{mab}(\mathbf{p}) P_{ia}(\mathbf{k}) P_{nb}(\mathbf{q}) f(k, q) E^*(k) E^*(q) \right. \\
 & \left. + \chi_q M_{nab}(\mathbf{q}) P_{ma}(\mathbf{p}) P_{ib}(\mathbf{k}) f(k, p) E^*(k) E^*(p) \} \right\}_{S_k}. \tag{A.19}
 \end{aligned}$$

Then, using eddy-damping and the Markovian process assumption, the kinetic energy equation finally reads

$$\begin{aligned}
 & \left[\frac{\partial}{\partial t} + 2v\chi_k^2 k^2 \right] E^*(k) = +8\pi k^2 \int_{\mathcal{O}^2} \Theta_{kpq}^{LES}(t) [-\chi_k^2 M_{imn}(\mathbf{k}) M_{iab}(\mathbf{k}) P_{ma}(\mathbf{p}) P_{nb}(\mathbf{q}) f(p, q) E^*(p) E^*(q) \\
 & + \chi_k \chi_p M_{imn}(\mathbf{k}) M_{mab}(\mathbf{p}) P_{ia}(\mathbf{k}) P_{nb}(\mathbf{q}) f(k, q) E^*(k) E^*(q) + \chi_k \chi_q M_{imn}(\mathbf{k}) M_{nab}(\mathbf{q}) P_{ma}(\mathbf{p}) P_{ib}(\mathbf{k}) f(k, p) E^*(k) E^*(p)] \delta_{\mathbf{k}-\mathbf{p}-\mathbf{q}} \mathbf{d}\mathbf{p} \mathbf{d}\mathbf{q} \\
 & + \left\{ 8\pi k^2 \sum_{\mathbf{a} \in \mathcal{A}_0} \int_{\mathcal{O}^2} \Theta_{kpq}^{LES}(t) [-\chi_k^2 M_{imn}(\mathbf{k}) M_{iab}(\mathbf{k}) P_{ma}(\mathbf{p}) P_{nb}(\mathbf{q}) f(p, q) E^*(p) E^*(q) \right. \\
 & \left. + \chi_k \chi_p M_{imn}(\mathbf{k}) M_{mab}(\mathbf{p}) P_{ia}(\mathbf{k}) P_{nb}(\mathbf{q}) f(k, q) E^*(k) E^*(q) + \chi_k \chi_q M_{imn}(\mathbf{k}) M_{nab}(\mathbf{q}) P_{ma}(\mathbf{p}) P_{ib}(\mathbf{k}) f(k, p) E^*(k) E^*(p)] \delta_{\mathbf{k}-\mathbf{p}-\mathbf{q}-\mathbf{a}} \mathbf{d}\mathbf{p} \mathbf{d}\mathbf{q} \right\}_{S_k}, \tag{A.20}
 \end{aligned}$$

where the triple correlation relaxation time is provided by

$$\Theta_{kpq}^{LES}(t) = \frac{1 - \exp(-\Xi_{kpq} t)}{\Xi_{kpq}} \tag{A.21}$$

with

$$\Xi_{kpq} = \mu_{kpq} + v(\chi_k^2 k^2 + \chi_p^2 p^2 + \chi_q^2 q^2) \tag{A.22}$$

and $\mu_{kpq} = \mu_k + \mu_p + \mu_q$ with the eddy-damping model given by (30).

The system is further simplified using the geometric coefficients x , y and z [32] defined by the following relationships:

$$x = -\frac{p_i q_i}{pq}, \quad y = -\frac{k_i q_i}{kq}, \quad z = -\frac{p_i k_i}{pk}. \tag{A.23}$$

At this point, the EDQNM-LES model reads

$$\left[\frac{\partial}{\partial t} + 2v\chi_k^2 k^2 \right] E^*(k) = T^{nl}(k) + T^{al}(k) \tag{A.24}$$

where the resolved nonlinear terms are defined by

$$T^{nl}(k) = \int \int_{\mathcal{A}_{k|kc}^{\leftarrow}} \Theta_{kpq}^{LES}(t) \left[\chi_k^2 \mathcal{L}_1(k, p, q) E^*(p) E^*(q) + \chi_k \chi_p \mathcal{L}_2(k, p, q) E^*(k) E^*(p) + \chi_k \chi_q \mathcal{L}_3(k, p, q) E^*(k) E^*(q) \right] \mathbf{d}\mathbf{p} \mathbf{d}\mathbf{q} \tag{A.25}$$

and the aliasing energy transfers read

$$T^{\text{al}}(k) = \left\{ \sum_{\mathbf{a} \in \mathcal{A}_0} \int \int_{\mathcal{A}_{|\mathbf{k}+\mathbf{a}|k_c}^{\leq}} \frac{k}{|\mathbf{k}+\mathbf{a}|} \Theta_{kpq}^{\text{LES}}(t) [\chi_k^2 \mathcal{L}_1(k, p, q) E^*(p) E^*(q) + \chi_k \chi_p \mathcal{L}_2(k, p, q) E^*(k) E^*(p) + \chi_k \chi_q \mathcal{L}_3(k, p, q) E^*(k) E^*(q)] dp dq \right\}_{S_k} \quad (\text{A.26})$$

with

$$\mathcal{L}_1(k, p, q) = \frac{k^3}{2pq} (1 - xyz - 2y^2z^2), \quad (\text{A.27})$$

$$\mathcal{L}_2(k, p, q) = -\frac{q^2}{2p} (xz + y^3), \quad (\text{A.28})$$

$$\mathcal{L}_3(k, p, q) = -\frac{p^2}{2q} (xy + z^3). \quad (\text{A.29})$$

The integration domain $\mathcal{A}_{|\mathbf{k}+\mathbf{a}|k_c}^{\leq}$ is defined in Section 3.4.1 and a sketch is provided in Fig. 1.

The last step consists in evaluating the spherical average of the aliasing term $T^{\text{al}}(k)$. Introducing

$$\mathcal{T}^{\text{al}}(\mathbf{k}, \mathbf{a}) = \int \int_{\mathcal{A}_{|\mathbf{k}+\mathbf{a}|k_c}^{\leq}} \frac{k}{|\mathbf{k}+\mathbf{a}|} \Theta_{kpq}^{\text{LES}}(t) [\chi_k^2 \mathcal{L}_1(k, p, q) E^*(p) E^*(q) + \chi_k \chi_p \mathcal{L}_2(k, p, q) E^*(k) E^*(p) + \chi_k \chi_q \mathcal{L}_3(k, p, q) E^*(k) E^*(q)] dp dq, \quad (\text{A.30})$$

we have

$$T^{\text{al}}(k) = \sum_{\mathbf{a} \in \mathcal{A}_0} \{ \mathcal{T}^{\text{al}}(\mathbf{k}, \mathbf{a}) \}_{S_k}. \quad (\text{A.31})$$

The sum over the aliasing modes \mathbf{a} is simplified by evaluating singly the contributions from 1D, 2D and 3D modes [6], so that

$$T^{\text{al}}(k) = \{ 6\mathcal{T}^{\text{al}}(\mathbf{k}, \mathbf{a}_{1\text{D}}) + 12\mathcal{T}^{\text{al}}(\mathbf{k}, \mathbf{a}_{2\text{D}}) + 8\mathcal{T}^{\text{al}}(\mathbf{k}, \mathbf{a}_{3\text{D}}) \}_{S_k}, \quad (\text{A.32})$$

which is equivalent to

$$T^{\text{al}}(k) = \frac{1}{4\pi} \int_0^{2\pi} \int_0^\pi [6\mathcal{T}^{\text{al}}(\mathbf{k}, \mathbf{a}_{1\text{D}}) + 12\mathcal{T}^{\text{al}}(\mathbf{k}, \mathbf{a}_{2\text{D}}) + 8\mathcal{T}^{\text{al}}(\mathbf{k}, \mathbf{a}_{3\text{D}})] \sin \varphi d\theta d\varphi, \quad (\text{A.33})$$

where $\mathbf{k} = (k \sin \varphi \cos \theta, k \sin \varphi \sin \theta, k \cos \varphi)$ and with vectors \mathbf{a} chosen arbitrarily. One may take for instance

$$\mathbf{a}_{1\text{D}} = (2k_c, 0, 0), \quad (\text{A.34})$$

$$\mathbf{a}_{2\text{D}} = (2k_c, 2k_c, 0), \quad (\text{A.35})$$

$$\mathbf{a}_{3\text{D}} = (2k_c, 2k_c, 2k_c). \quad (\text{A.36})$$

The calculation of the spherical averaging in (A.33) is performed numerically using the following algorithm:

$$T^{\text{al}}(k) = \frac{1}{4\pi} \sum_{\theta_i, \varphi_j} [6\mathcal{T}^{\text{al}}(\mathbf{k}, \mathbf{a}_{1\text{D}}) + 12\mathcal{T}^{\text{al}}(\mathbf{k}, \mathbf{a}_{2\text{D}}) + 8\mathcal{T}^{\text{al}}(\mathbf{k}, \mathbf{a}_{3\text{D}})] \sin \varphi_i \Delta \varphi \Delta \theta \quad (\text{A.37})$$

with

$$\begin{aligned} \theta_i &= (i-1) \frac{\pi}{n_p} \quad \text{for } i = 1, \dots, 2n_p + 1, \\ \varphi_j &= (j-1) \frac{\pi}{n_p} \quad \text{for } j = 1, \dots, n_p + 1 \end{aligned} \quad (\text{A.38})$$

and $\Delta \theta = \Delta \varphi = \pi/n_p$. Such an approach may be demanding in terms of computational resources but it appears that taking $n_p = 10$ is enough to provide accurate results. The aliasing energy transfer $T^{\text{al}}(k)$ evaluated with (A.37) is for instance shown in Fig. A.4 as a function of k for $n_p = 10$ and for $n_p = 100$, for spectral numerical methods ($\chi_k = 1$ for every k). The two results are seen to collapse very well, thus ensuring that taking $n_p = 10$ is enough to capture the features of the aliasing energy transfer.

A.4. LES with spectral eddy viscosity

Subgrid scale modeling with spectral eddy viscosity can be easily introduced into the EDQMN-LES since the turbulent eddy viscosity acts as a diffusive term with a viscosity $\nu_t = \nu_t(k)$ depending on the wavenumber. We are then left with

$$\left(\frac{\partial}{\partial t} + 2\nu_t k^2 + 2\nu \chi_k^2 k^2 \right) E^*(k) = T_{\text{nl}}(k) + T_{\text{al}}(k). \quad (\text{A.39})$$

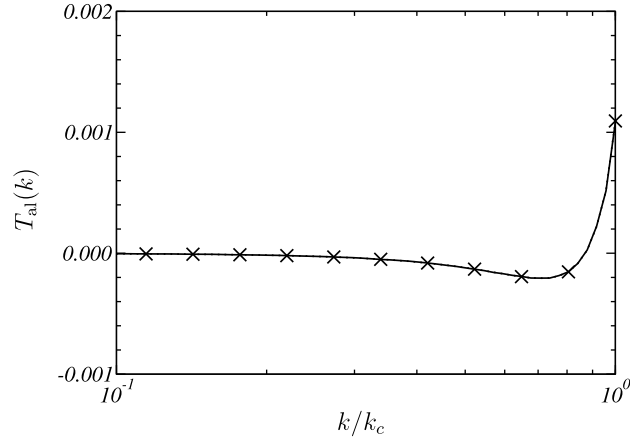


Fig. A.4. Energy transfer $T_{al}(k)$ due to the aliasing effects at $t^* = 8$ as a function of k/k_c , provided by the EDQNM-LES calculations for $Re_\lambda = 2500$ and $k_c = 32$, with spectral differentiation. Number of points used for averaging over the shell of radius k : —, $n_p = 10$; — \times —, $n_p = 100$.

To avoid any discussion on the interplay between the numerics and the SGS model, it is assumed that the approximate differentiation and the grid projection do not have any influence on the spectral eddy viscosity term.

Appendix B. Asymptotic development of the differentiation error for small wavenumbers

An asymptotic development of the differentiation error $\mathcal{E}_{fd}(k)$ is provided in order to account for the decrease in k^5 of the error spectrum for low wavenumbers pointed out in Section 4.3.1.

According to Eq. (39), the differentiation errors are given by

$$\mathcal{E}_{fd}(k) = |T_{nl}(k) - T^<(k|k_c)| + |2\nu k^2[E(k) - \chi_k^2 E^*(k)]|, \quad (B.1)$$

where the resolved energy transfers of the EDQNM-DNS model are provided by

$$T^<(k|k_c) = \int \int_{\mathcal{A}_{k|k_c}^<} S(k, p, q) dp dq \quad (B.2)$$

with

$$S(k, p, q) = \Theta_{kpq}(t)[\mathcal{L}_1(k, p, q)E(p)E(q) + \mathcal{L}_2(k, p, q)E(k)E(p) + \mathcal{L}_3(k, p, q)E(k)E(q)]. \quad (B.3)$$

The above definition for $S(k, p, q)$ is equivalent to the one given by Eq. (26) [16]. It is used here because this expression is very similar to the equation for the resolved energy transfers $T_{nl}(k)$ of the EDQNM-LES model in Appendix A.3:

$$T^{nl}(k) = \int \int_{\mathcal{A}_{k|k_c}^<} \Theta_{kpq}^{LES}(t)[\chi_k^2 \mathcal{L}_1(k, p, q)E^*(p)E^*(q) + \chi_k \chi_p \mathcal{L}_2(k, p, q)E^*(k)E^*(p) + \chi_k \chi_q \mathcal{L}_3(k, p, q)E^*(k)E^*(q)] dp dq. \quad (B.4)$$

It is now assumed that the kinetic energy spectrum of the EDQNM-DNS and EDQNM-LES models, as well as the triple relaxation correlation times $\Theta_{kpq}(t)$ and $\Theta_{kpq}^{LES}(t)$, are equal.

For the sake of simplicity, an approximate differentiation scheme of infinite order of accuracy is considered. Its isotropic modified wavenumber ratio is artificially defined by

$$\chi_k = 1 - \delta_{k-k_c}, \quad (B.5)$$

where δ is the Dirac delta function. Such an algorithm resolves perfectly all the wavenumbers (i.e. $\chi_k = 1$) apart from the cut-off wavenumber k_c , for which $\chi_{k_c} = 0$. An infinite order of accuracy numerical method is idealistic but this is however an interesting limit case of the finite-order finite-difference schemes.

According to (B.5), the differentiation error then reads, for $k < k_c$

$$\mathcal{E}_{fd}(k) = |\Theta_{kk_c k_c}(t)E(k)E(k_c)[\mathcal{L}_2(k, k_c, k_c) + \mathcal{L}_3(k, k_c, k_c)]|. \quad (B.6)$$

The behaviour of $\mathcal{E}_{fd}(k)$ is now investigated for $k \rightarrow 0$. Based on Eq. (29), it is straightforward to demonstrate that the triple relaxation time $\Theta_{kk_c k_c}(t)$ converges towards a constant non-zero value when k tends to zero. In addition, the kinetic energy spectrum is such as $E(k) \sim k^4$ for $k \ll 1$ [16], so that

$$\mathcal{E}_{fd}(k) \sim k^4 |\mathcal{L}_2(k, k_c, k_c) + \mathcal{L}_3(k, k_c, k_c)| \quad (B.7)$$

with using (A.28) and (A.29)

$$\mathcal{L}_2(k, k_c, k_c) \sim xz + y^3, \quad (\text{B.8})$$

$$\mathcal{L}_3(k, k_c, k_c) \sim xy + z^3. \quad (\text{B.9})$$

Applying the scalar product inside the triangle $(\mathbf{k}, \mathbf{p}, \mathbf{q})$ permits to show that

$$x = -\frac{k^2 - p^2 - q^2}{2pq}, \quad (\text{B.10})$$

$$y = -\frac{p^2 - k^2 - q^2}{2kq}, \quad (\text{B.11})$$

$$z = -\frac{q^2 - p^2 - k^2}{2pk}. \quad (\text{B.12})$$

As a result, for $k \rightarrow 0$ and $p = q = k_c$, we have

$$x \sim 1, \quad y \sim k, \quad z \sim k, \quad (\text{B.13})$$

so that $xz \sim k$ and $xy \sim k$ are the leading terms in $\mathcal{L}_2(k, k_c, k_c)$ and $\mathcal{L}_3(k, k_c, k_c)$, respectively.

Finally, for small wavenumbers, the differentiation errors are given by

$$\mathcal{E}_{\text{fd}}(k) \sim k^5. \quad (\text{B.14})$$

This asymptotic development is consistent with the results obtained for the finite-order schemes in Section 4.3.1, and observed for instance in Fig. 8.

References

- [1] P. Sagaut, Large-eddy simulation for incompressible flows – an introduction, third ed., Scientific Computation Series, Springer-Verlag, 2005.
- [2] J. Smagorinsky, General circulation experiments with the primitive equations: I. The basic experiment, *Mon. Weather Rev.* 91 (1963) 99–163.
- [3] M. Lesieur, O. Métais, New trends in large-eddy simulations of turbulence, *Annu. Rev. Fluid Mech.* 28 (1996) 45–82.
- [4] S. Pope, Ten questions concerning the large-eddy simulation of turbulent flows, *New J. Phys.* 6 (2004) 1–24.
- [5] C. Tam, Computational aeroacoustics: issues and methods, *AIAA J.* 33 (1995) 1788–1797.
- [6] S. Ghosal, An analysis of numerical errors in large-eddy simulations of turbulence, *J. Comput. Phys.* 125 (1996) 187–206.
- [7] N. Park, K. Mahesh, Analysis of numerical errors in large eddy simulation using statistical closure theory, *J. Comput. Phys.* 222 (2007) 194–216.
- [8] F. Chow, P.A. Moin, A further study of numerical errors in large-eddy simulations, *J. Comput. Phys.* 184 (2003) 366–380.
- [9] A. Kravchenko, P. Moin, On the effect of numerical errors in large eddy simulations of turbulent flows, *J. Comput. Phys.* 131 (1997) 310–322.
- [10] G. Comte-Bellot, S. Corrsin, Simple Eulerian time correlation of full- and narrow band velocity signals in grid-generated, ‘isotropic’ turbulence, *J. Fluid Mech.* 48 (1971) 273–337.
- [11] C. Bogey, C. Bailly, A family of low dispersive and low dissipative explicit schemes for flow and noise computations, *J. Comput. Phys.* 194 (2004) 194–214.
- [12] J. Domaradzki, N. Adams, Direct modelling of subgrid scales of turbulence in large eddy simulations, *J. Turbulence* 3 (2002) 1–19.
- [13] F.N. Felten, T.S. Lund, Kinetic energy conservation issues associated with the collocated mesh scheme for incompressible flow, *J. Comput. Phys.* 215 (2006) 465–484.
- [14] J. Meyers, B.J. Geurts, P. Sagaut, A computational error-assessment of central finite-volume discretizations in large-eddy simulation using a Smagorinsky model, *J. Comput. Phys.* 227 (2007) 156–173.
- [15] T.S. Lund, H.-J. Kaltenbach, Experiments with explicit filtering for LES using finite-difference method, *Annual Research Briefs 1995*, Center for Turbulence Research, NASA Ames/Stanford Univ., 1995, pp. 91–105.
- [16] M. Lesieur, *Turbulence in Fluids*, Kluwer Academic, 1987.
- [17] J.-P. Chollet, M. Lesieur, Parametrization of small scales of three-dimensional isotropic turbulence utilizing spectral closures, *J. Atmos. Sci.* 38 (1981) 2747–2757.
- [18] C. Leith, Atmospheric predictability and two-dimensional turbulence, *J. Atmos. Sci.* 28 (1971) 145–161.
- [19] O. Schilling, Y. Zhou, Analysis of spectral eddy viscosity and backscatter in incompressible, isotropic turbulence using statistical closure theory, *Phys. Fluids* 14 (3) (2002) 1244–1258.
- [20] M. Germano, U. Piomelli, P. Moin, W. Cabot, A dynamic subgrid-scale eddy viscosity model, *Phys. Fluids A* 3 (7) (1991) 1760–1765.
- [21] M. Salvetti, F. Beux, The effect of the numerical scheme on the subgrid scale term in large-eddy simulation, *Phys. Fluids* 10 (1998) 3020–3022.
- [22] S. Hickel, N. Adams, J. Domaradzki, An adaptive local deconvolution method for implicit LES, *J. Comput. Phys.* 213 (2006) 413–436.
- [23] J.-P. Chollet, Two-point closures as a subgrid-scale modeling tool for large-eddy simulations, in: F. Durst, B.E. Launder (Eds.), *Turbulent Shear Flows IV*, Springer, Heidelberg, 1984, pp. 62–72.
- [24] R. Kraichnan, Eddy viscosity in two and three dimensions, *J. Atmos. Sci.* 33 (1976) 1521–1536.
- [25] J. Mathew, R. Lechner, H. Foysi, J. Sesterhenn, R. Friedrich, An explicit filtering method for large eddy simulation of compressible flows, *Phys. Fluids* 15 (8) (2003) 2279–2289.
- [26] M.R. Visbal, D.V. Gaitonde, Higher-order-accurate methods for complex unsteady subsonic flows, *AIAA J.* 37 (10) (1999) 1231–1239.
- [27] C. Bogey, C. Bailly, Large Eddy Simulations of transitional round jets: influence of the Reynolds number on flow development and energy dissipation, *Phys. Fluids* 18 (2006) 1–14. #065101.
- [28] J. Berland, C. Bogey, C. Bailly, Investigation using statistical closure theory of the influence of the filter shape on scale separation in large-eddy simulation, *J. Turbulence*, submitted for publication.
- [29] C. Bogey, C. Bailly, On the application of explicit spatial filtering to the variables or fluxes of linear equations, *J. Comput. Phys.* 225 (2007) 1211–1217.
- [30] J. Gullbrand, F.K. Chow, The effect of numerical errors and turbulence models in large-eddy simulations of channel flow with and without explicit filtering, *J. Fluid Mech.* 495 (2003) 323–341.
- [31] O.V. Vasilyev, T.S. Lund, P. Moin, A general class of commutative filters for LES in complex geometry, *J. Comput. Phys.* 146 (1998) 82–104.
- [32] S. Orszag, Analytical theories of turbulence, *J. Fluid Mech.* 41 (1970) 363–386.